POLITECNICO DI TORINO

Environmental and Land Engineering

CLIMATE CHANGE

Master's Degree Thesis

A study on the dynamics of an Alpine Lake: the Seracchi Lake case

Supervisors

Prof. Stefania TAMEA

Prof. Carlo CAMPOREALE

Elisabetta CORTE

Candidate

Martina VISCIDO

July 2023

Abstract

In the context of the ongoing climate change, there is an increasing urgency and interest in characterizing the mountain environment and gaining a deeper understanding of its dynamics. This is particularly important in the Alps, where the increase in average air temperature has doubled the average global temperature increase. To address this pressing issue, the CC-Glacier Lab was established at the Politecnico di Torino in 2021, with a focus on studying and characterizing the Rutor Glacier and its proglacial area in the Aosta Valley region, Italy. This thesis was conducted under the supervision of the hydrological team working with the CC-Glacier Lab, with the aim of improving knowledge about the largest proglacial lake in the area, known as Seracchi Lake (Lago dei Seracchi).

By means of geomatic, geophysical, and hydrological data collected over two years (2021 and 2022), this thesis provides valuable insights into the morphology and hydrology of the lake. The research includes the reconstruction of the lake's bathymetry, the elaboration of surface area-water level and volume-water level curves, and the determination of the water budget. In particular, the accurate reconstruction of the inflow time series, which was challenging to measure directly due to the rugged nature of the area, is a significant achievement of this study.

These findings have proven useful to obtain a deeper understanding of the link between hydrological dynamics and temperature as well as hydrological dynamics and precipitation conditions. The correlation between maximum and mean inflows with temperature is investigated, and the days with precipitation events are studied separately from the days without precipitation. Three parameters are calculated to characterize the lake dynamics: the difference between the maximum inflow and the maximum outflow value, the time delay between the two values, and the retention volume.

A comparative analysis between the reference summer of 2021 and the notably dry summer of 2022 reveals that, on average, the retention volume was 82% higher than in 2021, and also the difference between the maximum inflow and outflow was 32% higher, while the time delay remained approximately the same. Moreover,

the general increase in Q_{IN} values which was recorded was probably related to an increase in glacier ablation. This might show the lake's potential as a proxy for glacier retreat.

In conclusion, this thesis represents an important first step in characterizing the studied area comprehensively. The methodology, results, and conclusions presented in this study contribute significantly to the understanding of the hydrological dynamics of Seracchi Lake and its implications in the context of climate change and glacier retreat. However, further investigations should be carried out without neglecting the importance of continuous monitoring and assessment of this alpine ecosystem.

"In verità, in verità io vi dico: se il chicco di grano, caduto in terra, non muore,
rimane solo; se invece muore, produce molto frutto."
Giovanni 12,24-26

Table of Contents

List of Tables

List of Figures

1 | Introduction

The planet Earth is currently facing the impacts of climate change, which are severely affecting the environment and human systems. The unprecedented rate at which GHGs are emitted into the atmosphere is irreversibly changing the climate, causing temperatures to become increasingly warmer, and the effects are more or less visible. The Cryosphere, the frozen component of the Earth system, is the physical compartment that exhibits the most rapid and visible changes [1].

Glaciers and ice sheets cover approximately 10% of the Earth's land area and play a crucial role in regulating the Planet's energy balance, storing freshwater, and supporting biodiversity. In 2019, the IPCC published the *'Special Report on The Ocean and Cryosphere in a Changing Climate'*, which highlighted the massive loss of ice mass from glaciers worldwide, the increasing permafrost temperatures, and the declining snow cover both in extension and duration, particularly at lower elevations [2].

The consequences related to the decline of glaciers, snow, and permafrost are significant. The mass loss exposes more land to sunlight and weathering. Land is not as white as glaciers or ice, which means lower albedo, higher absorbed radiations and rising temperatures. Moreover, the retreat of glaciers contributes to decreasing the stability of mountain slopes and compromises the integrity of infrastructures. It also alters the frequency, magnitude, and location of natural hazards [2]. Glacier melting and changes in precipitation patterns also change the amount and seasonality of runoff in snow-dominated and glacier-fed river basins. Stating to IPCC,it has been observed an increase in winter runoff, as a result of increased air temperatures and related shifts from solid to liquid precipitation. There is also an increase in summer runoff due to intensified glacial melting, except for those areas dominated by small glaciers, such as European Alps [2]. In this areas it may happen that the glaciers due to their limited extension have already experienced the maximum shrinking rate possible. In this cases it is recorded a decrease both in shrinking and summer runoff.

Therefore, mountain regions are likely to be more vulnerable than other areas to the impacts of climate change, which can have a significant effect on both the environment and the livelihoods of the people.
Among all mountain environments, the European Alps are highly exposed to climate change as the increase in average air temperature has doubled the average global temperature increase [3], with different warming trends at various elevations. Moreover, the duration of sunshine has increased by about 15% since the 1980s [3]. According to the article *The European mountain cryosphere: a review of its current state, trends, and future challenges* [1], by 2100 Europe's mountain cryosphere will undergo notable transformations, characterized by the disappearance of low- and mid-altitude glaciers, retreat and mass loss of even large valley glaciers, the disappearance of permafrost at lower elevations and its warming at higher elevations. As a result, the tree line will shift upward and vegetation will expand to current periglacial areas, the timing of maximum discharge will change, with a transition of runoff regimes from glacial to nival and nival to pluvial and there will be unprecedented mass movements and process chains.

The decrease in European mountain glaciers is expected to continue because they are not in balance with the climate. In many cases this is due to the limited altitude of the glaciers, which prevents them from reaching a new equilibrium with the climate, even if air temperatures will have stabilized by the end of the century [1].
The authors Zekollari et al. [4] investigated the loss of glacier mass in the European Alps under different concentration pathways. Their findings reveal that by the end of the century, the strongest RCP scenario would result in the loss of $94 \pm 4\%$ of the 2018 glacier volume. Even in the best-case scenario regarding emissions limitations,RCP2.6, the reduction in glacier volume may be only limited to two-thirds of the volume present in 2018.

Therefore, studying the impacts of climate change on the Alps is of paramount importance, not only to understand the changes but also to develop sustainable strategies to adapt to and mitigate their consequences on local communities and the environment.

1.1 Problem statement

The process of deglaciation is transforming the appearance of mountain landscapes, as glaciers are receding and giving way to newly formed proglacial lakes and loose, unconsolidated debris known as moraine material.

Proglacial lakes are bodies of water located near the edge of a glacier or influenced by melting glacier ice on land. The size, morphology, hydrology, and persistence of these lakes are strongly linked to their proximity to glaciers [5].
They are usually shallow, with a bathymetry marked by submerged bedrock hills and depositional landforms and they can experience rapid changes in water level due to the influx of glacial meltwater. The bathymetry is the primary factor responsible for sediment dispersal assisted by the water level which determines the oxygen and thermal stratification of the lake and in turn, affect the mixing potential of the water and sediments.

Periglacial lakes play a crucial role in interrupting and slowing down the flow of meltwater, enabling sedimentation. Quantifying the amount of sediment that a lake is capable of trapping is important not only for understanding the lake's evolution but also for comprehending the evolution of the surrounding area. Moreover, the sediment stratification in proglacial lakes provides valuable information about short-term inter-seasonal patterns, inter-annual patterns, and long-term patterns of glacier-derived meltwater fluctuations [5]. Lake stratification serves as proxy evidence for regional hydrological changes and climate variability.

In addition to their significance in the geological and hydrological processes, proglacial lakes can also have a substantial impact on the local and global climate. During the summer, they absorb relatively high amounts of incoming shortwave radiations due to a lower albedo than the surrounding environment. During winter, they freeze and reflect most incoming shortwave radiations. Moreover, they retain cold meltwater and have a greater thermal heat capacity than the surrounding land. These factors combined lead to relatively cool summer air temperatures, which, in turn, retard summer ice ablation.

Over the past few decades, there has been a rapid increase in both the quantity

and size of proglacial lakes [6].
The formation of new bodies of water in proglacial areas can have positive implications for preserving biodiversity and storing freshwater. However, there are also associated risks such as the destabilization of slopes which can lead to landslides. In addition, sudden water outbursts can occur due to rock/ice avalanches or mass movements [3]. These events in the Alps are even more dangerous, due to the proximity to urban agglomerations and infrastructures [7].

So, periglacial lakes are an essential element in the deglaciation process, offering a valuable resource for data sampling and understanding glacial processes,and at the same time their persistence is strongly affected by glacial melting. Therefore, it is important to study their behavior and characteristics.

Although recent improvements have been made in this field of study, new dynamics and associated concerns have led to an emerging area of research focused on quantitatively understanding the interactions between lakes and glaciers [8].
Despite their role as a temporary storage for meltwater is well known, this process has been disregarded in models that address the hydrological reaction of glaciers to climate change and the computation of sea level rise [6]. The main obstacle to quantifying the contributions of lakes to glacier dynamics is the lack of data in spatial and temporal coverage. For example, there has been no a worldwide assessment of glacial lake size or capacity, resulting in limited information on the amount of water stored in these lakes and the temporal trend of glacial lake storage.
The author Carravick [8] suggests several questions that must be addressed, such as whether meltwater from diminishing glaciers is causing the lakes to grow, whether the lakes are accelerating glacier shrinkage, or whether a combination of both is responsible and what the balance between these processes is.

Summarising, the study of proglacial lakes is a critical area of research. The recent increase in the quantity and size of proglacial lakes highlights the urgency of understanding the interactions between lakes and glaciers. By studying these processes in greater detail, it is possible to gain important insights into the physical dynamics and work towards more effective solutions for mitigating the impacts of climate change and build adaptation strategies.

1.2 Literature on the theme

The alteration processes affecting the proglacial area have opened up new research fields. In the last 20 years, there has been significant scientific attention focused on characterizing deglaciation processes and quantifying the effects of these changes. Numerous branches of study are involved in these investigations, offering various approaches.
When examining the literature on climate change-related issues in proglacial areas, particularly in the Alps, a substantial number of articles have been published. The research focuses within this field are highly diverse.

Extensive research has been conducted on the geomorphology of the Alpine environment. For example, many authors have examined variations in glacial coverage and tracked changes in glacier extension. Historical descriptions of the study area are fundamental when available, but the greatest contribution comes from geomatics. The availability of high-resolution topographic surveys covering different years allows for a multitemporal analysis for example by building accurate Digital Elevation Models of difference (DoDs). This kind of products allow the calculation of volumes of erosion and deposition, as explained in the article by Savi et al. [9].

When studying morphological changes, one crucial aspect to analyze, beyond variations in glacier volume, is the sediment budget. Since deglaciated areas are more exposed to erosion, a greater amount of sediment can be produced and transported downstream by glacial meltwater, runoff, and wind. Quantifying the sediment budget is essential for understanding the potential effects of any changes that may occur.
Another facet of morphological investigation pertains to the study of the appearance or disappearance of certain features, such as proglacial lakes. These studies aim to characterize the proglacial lakes and understand the environmental conditions that favor their formation. Based on this knowledge, some authors attempt to develop models capable of predicting the formation and location of new proglacial lakes based on the expected glacier changes.

Together with morphology, the hydrological aspect is of primary interest as well.

There is an extensive literature on glacial hydrology. However, two interesting topics that are less commonly addressed are worth noting. The first topic, covered by Müller [10], explores the specific hydrological behavior of landforms that develop after glacier retreat within and near proglacial margins. The author seeks to document the hydrological functioning of these landforms using appropriate metrics, propose a framework for characterizing the timing, amount, and location of different water sources (rain, snow, ice) in these landforms and between them, and examine whether the documented response of individual landforms can explain observed catchment-scale behavior in terms of streamflow amounts, timing, and geochemistry. The other less-covered topic regards how changes in surface cover can affect the partitioning of precipitation into overland flow and infiltration, a problem studied by Maier and van Meerveld [11].

Additionally, many authors explore the relationship between observable physical changes and temperature and precipitation, for example, by studying the data in the frequency domain.

Tracking these changes is not only necessary for quantification and understanding future expectations but also because they are already occurring. It is crucial to approach them with a focus on potentiality and to develop advantageous adaptation strategies. In light of these considerations, the article *'Glacier tourism and climate change: effects, adaptations, and perspectives in the Alps'* is recommended [12]. As stated by the author of the article, research on the effects and adaptations of glacier tourism to climate change is scarce in Europe. This article offers an interesting overview of the physical processes that affect glacier tourism in the Alps and how stakeholders perceive and adapt to them.

1.3 The goal of the study

The topic of this thesis falls within the broad research area dedicated to periglacial lakes and specifically focuses on the characterization of the alpine lake noted as Lago dei Seracchi (from now on Seracchi Lake), located in the Rutor Glacier's periglacial area in Aosta Valley, Italy (Figure 2.1).

The work has been supervised by the hydrological research group of the "CC-Glacier Lab", a multisite laboratory established as part of the MIUR project "Department of Excellence" at Politecnico di Torino - DIATI.

Since 2020, the research group has made significant efforts to collect a comprehensive data-set on the lake. The main objective of this thesis is to utilize all the available data to reconstruct the lake's morphology and hydrology, providing valuable insights into its fundamental dynamics. Key questions to be addressed include estimating the volume of water retained, determining the inflow rates and understanding how the lake's behavior varies throughout the year and between different years.

The hydrological characterization of the lake not only contributes to gaining a comprehensive understanding of the study area but also serves as an indicator of the changes occurring in the glacier. It is essential to identify and analyze the changes in the lake dynamics that may be influenced by glacier retreat, aiming to unravel the cause-and-effect relationships between the glacier and the lake.

However, it is important to acknowledge that this thesis represents just the initial step in the research. To achieve a more comprehensive understanding, additional information, such as the sediment budget, will be necessary. Indeed, further investigations into the lake's sediment dynamics will provide valuable insights into the overall functioning and response of the system to environmental changes.

2 | The site

2.1 The Aosta Valley glaciers and the CC-Glacier Lab

The Alps are a remarkable region that serves as a natural observatory for studying the impacts of climate change on natural systems. By understanding the dynamics of the processes going on in this region, it is possible to gain important insights into the mechanisms driving the shifts and better understand the potential long-term impacts.

Focusing on the Italian Alps, the Aosta Valley stands out as the region with the largest glacier coverage [13]. Glaciers in this area not only serve as vital freshwater sources but also hold significant cultural and touristic value, with local communities deeply intertwined with glacier dynamics.

Research conducted by Viani [13] attests the ongoing trend of deglaciation. A comparison between the Italian Glacier Inventory data from 2005 to 2011 and the data collected in 1991 reveals an increase in the number of glaciers from 183 to 192, however the total covered area has decreased from 163.1 km^2 to 133.7 km^2. These glaciers could be found at elevations ranging from 1 400 m above sea level to 4 800 m above sea level, with a predominance of small glaciers. The study indicates that only 15 glaciers were larger than 3 km^2, accounting for approximately 80% of the total glacier area. Among them, the largest glaciers in 1991 were Miage (13.6 km^2), Lys (11.8 km^2), and Rutor (9.3 km^2).

In a recent study [14] the same author highlights also the formation of around 337 new glacier lakes within the boundaries of the Little Ice Age (LIA) glaciers extent, mainly localized in the Rutor-Lechaud chain. Once again, despite the high number of these lakes, they are small in size. Notably, lakes such as Miage (Veny Valley) and Blue (Ayas Valley) serve as important tourist attractions and valuable geosites due to their geological and geomorphological significance. However, certain lakes, including Rutor and Miage, have been identified as potentially hazardous

[13].

In light of this context, at the at Politecnico di Torino - DIATI it is born the "CC-Glacier Lab", as part of the MIUR project "Department of Excellence". The CC-Glacier Lab is a multisite laboratory with the primary objective of identifying and analyzing the dynamics taking place in periglacial areas that are currently experiencing deglaciation processes and associated mass movements. The specific study area chosen for investigation is the Rutor Glacier and its periglacial area, located in the Aosta Valley, Italy.

The significance of this work lies in its interdisciplinary nature, bringing together researchers from hydrology, geophysics, geomatics, and water engineering. Moreover, since its inception in 2021, the project has involved extensive data collection efforts in the area, combining on-field survey campaigns and long-term monitoring. Instruments have been installed throughout the site to gather data spanning the entire melting season over multiple years, allowing for a multi-temporal characterization of the area.

The CC-Glacier Lab project offers a distinctive opportunity to acquire valuable insights into the transformations taking place in the Alps as a result of climate change. Furthermore, the knowledge gained through this research can contribute to the development of effective strategies for both mitigating the impacts of climate change and adapting to its consequences.

2.2 The Rutor Glacier

The Rutor Glacier is located in the Rutor-Lechaud chain within the Graian Alps in NW Italy and extends into French territory (Figure 2.1). It is the third largest glacier in the Aosta Valley region [13].

To gain a comprehensive understanding of the glacier's evolution, it is necessary to start from the period known as the Little Ice Age. Spanning from the 14th to the 19th centuries, this era was characterized by a considerable drop in global temperatures [13]. Consequently, glaciers, including the Rutor, experienced substantial growth and reached their maximum expansion.

Luckily, a substantial body of documented research about the history of the Rutor Glacier is available (see the article [15] for a detailed reconstruction) and also the glacier itself provides compelling evidence of its evolution. Based on this information, it is known that the Rutor Glacier's maximum expansion is dated back to 1864 [13, 16]. The configuration of the glacier at its maximum expansion serves as a reference point for comparing the present conditions [16]. Figure 2.3, taken from the Vergnano's article [15] shows a reconstruction of the glacier front historical evolution.

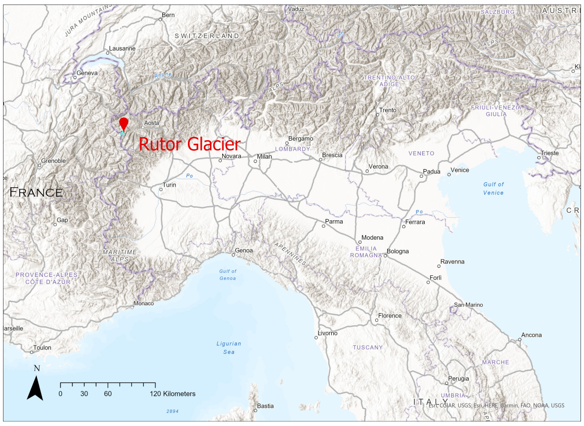

Figure 2.1: Highlight of Rutor glacier location respect to NW Italy. Base map by ESRI.

The Rutor morphology is relatively flat, characterized by a combination of steep rocky ledges and sub-flat basins [13, 16]. In the upper section, a rocky ridge divides the glacier into two branches, which later converge in the lower part. The glacier terminates in three tongues at its front [13]. Figure 2.2 provides a visual representation of the glacier's appearance in 2012. However, it is important to note that the altitude and aspect of the glacier may vary depending on its extension. Since the Little Ice Age (LIA), when the glacier had a surface area of approximately 12 km^2 [17], there have

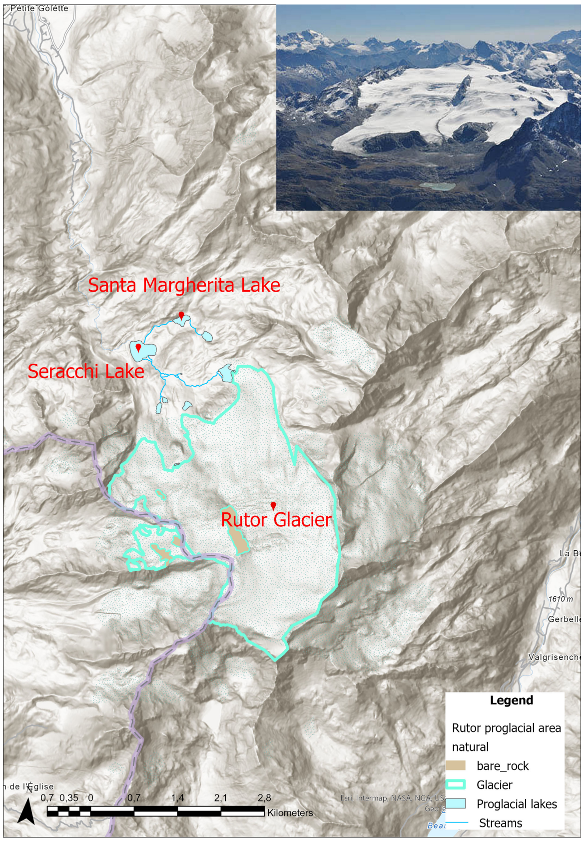

Figure 2.2: Zoom on the Rutor proglacial area. In the map the contour of the glacier and of the main proglacial lakes are highlighted. The features are taken from Open Street Map website. The aerial picture of the glacier is from Nimbus website.

been significant changes in its extension, as clearly depicted in Figure 2.3.

Currently, the glacier covers an area of about 7.9 km^2 [18] and its altitude ranges between 2 540 - 3 486 m above sea level [18].

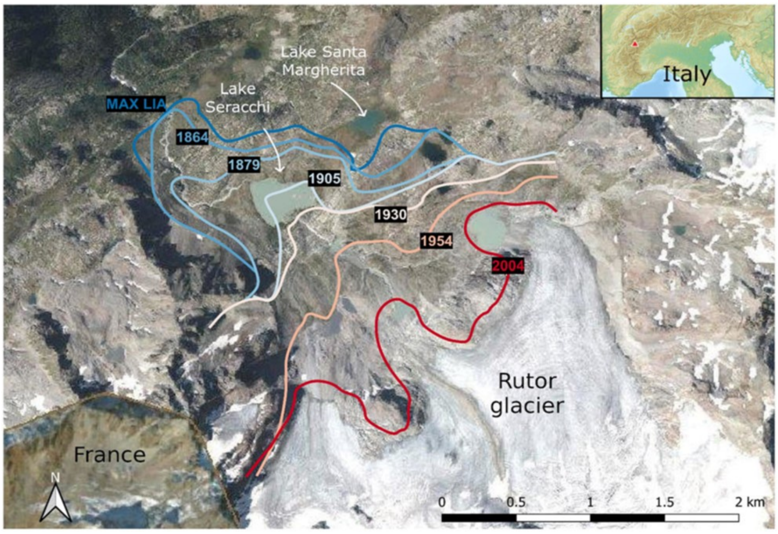

Figure 2.3: Evolution of the Rutor Glacier front starting from the Little Ice Age (LIA) configuration (picture source: [15]).

2.2.1 Mass Balance

The snow accumulation and melting cycle of the Rutor Glacier have been extensively studied and documented thanks to the monitoring efforts and sampling campaigns conducted by ARPA, the Aosta Valley regional agency for environmental protection.

Since 2005, the agency has been using the collected information to assess the annual mass variation of the glacier, which serves as an indicator of the impacts of climate change. This variation is expressed in mm of water equivalent and is determined by calculating the net mass balance between winter - spring accumulation and summer ablation [19]. Winter and spring accumulation are assessed by measuring the snow height and ice density at specific points towards the end of spring, while the summer ablation is determined by observing the melting of snow and ice, either directly by measuring the surface lowering using rods embedded in the ice, or indirectly by comparing Digital Surface Models from different years [19].

The mass balance data are updated to 2022, a year characterized by a dry winter and a prolonged and severe ablation period [20]. As a result, glaciers in the Aosta Valley experienced significant retreat. However, compared to other glaciers in the region, the Rutor had a higher accumulation due to the contribution of Atlantic disturbances coming from the French slope [20].

Figure 2.4 illustrates the results of the entire monitoring period. It is evident that the winter of 2022, with a total accumulation of 1 077 mm of water equivalent [21], ranked as the sixth in terms of mass shortage. Additionally, in this year it has been recorded the highest ablation value throughout the monitoring period. By July 2022, the ablation registered for the entire hydrological year of 2020-2021 had already been reached [21].

In the end, the net mass balance for the 2021-2022 period resulted in -4.946 mm of water equivalent, with a retreat of 31 – 40 m for the right tongue, 27 m for the left and 26 m for the central one. [21].

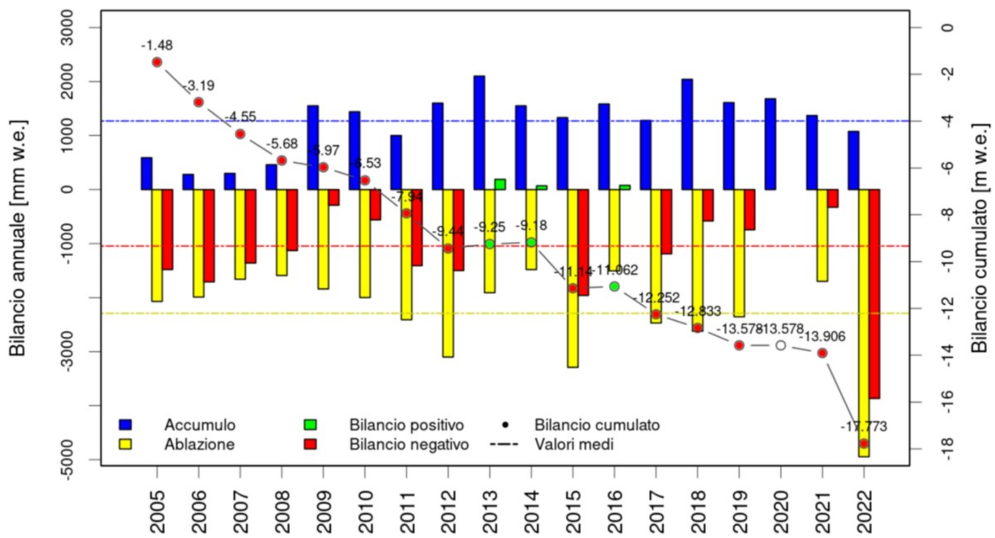

Figure 2.4: Rutor yearly mass balance for the period 2005-2022. The mass balance is calculated as winter - spring accumulation minus summer ablation (source ARPA VdA [21]).

2.3 Rutor proglacial area and the Seracchi Lake

The Rutor proglacial area has undergone significant expansion since the Little Ice Age as a result of glacier retreat [17]. The deglaciated region exhibits numerous topographic depressions, which have been predominantly filled with glacial sediments and meltwater, giving rise to the formation of new proglacial lakes.

These changes in the hydrological system have had an impact on the stream network as well [18]. The change can be easily observed by comparing the network depicted in Figure 2.3, which is based on data from the Open Street Map website, to the most recent and accurate description of the stream network and the area provided by the CC-Glacier Lab work group. According to Corte [18], the glacier currently feeds five lakes, two of which have formed within the last five years and are directly connected to the glacier lobe.

All the meltwater output from these lakes, ultimately find its way into Seracchi Lake (also known as Rutor Lake in literature), located at the lowest point of the proglacial area, approximately 2 387 m above sea level. The history of this lake is relatively recent, as it was born around 1880-1920 [15] and it was the first lake to form in the area [14].
In terms of surface area, it ranks as the third-largest lake in the Aosta Valley [14].

The inflow from the glacier enters the lake from the south, while there is a second inflow from Santa Margherita Lake (2 422 m above sea level) in the northeastern part, see Figure 2.5. The outflow, known as the Rutor Torrent, is situated in the northern part of the lake.

The presence of Seracchi Lake not only serves as a testament to the historical glacial activity in the region but also highlights the ongoing changes driven by climate change. Under the new climate conditions, variations in the water and sediment budget of the lake become increasingly likely, posing the risk of catastrophic events and irreversible transformations.

The entire area is highly susceptible to changes in morphology and hydrological dynamics. The Seracchi Lake has a distinctive greyish color (see Figure 2.6) precisely caused by its significant sediment budget. So, the combination of increased sediment

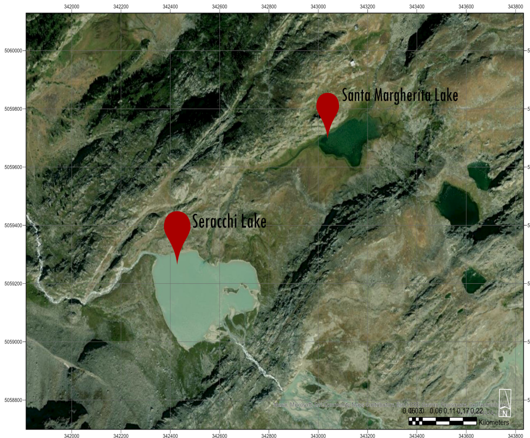

Figure 2.5: Santa Margherita location in respect to Seracchi lake. Base Map by ESRI.

Figure 2.6: Seracchi Lake picture, taken facing north (online source).

input, due to enhanced erosion and a higher presence of moraine material, along with the lake's specific morphology, could contribute to its potential disappearance in the future [15].
Additionally, the Santa Margherita marginal lake has been already subjected to repeated flood events since the 16th century, and these events have been thoroughly documented [17].

The concerns surrounding the dynamics of Seracchi Lake are further underscored by the research conducted by Viani [17], who examined the hazards associated with proglacial lakes in the Alps. Notably, Seracchi Lake received the highest score in terms of its interaction with human activities and its proximity to populated areas. The area attracts frequent visitors, particularly due to the presence of the popular hiking trail (Alta Via n. 2) and the Deffeyes Hut [14]. Furthermore, Santa Margherita Lake also holds religious significance. In response to the outburst events, a chapel was constructed on a promontory overlooking the lake in 1937, serving as a place of devotion and protection against the devastating floodwaters. To this day, an annual Holy Mass is held at the chapel [14].

The susceptibility of the lake to sediment transport, the potential for catastrophic events, and its proximity to human activities highlight the need for ongoing research, monitoring, and management efforts to mitigate risks and ensure the

long-term sustainability of the area.
However, research activities also have the responsibility to explore new possibilities that arise from these changes. This includes investigating the potential for increased availability of freshwater resources and studying the dynamics to adapt livelihoods accordingly. By viewing the environment as a valuable resource that needs protection, it is possible to foster harmony between human activities and the natural surroundings.

3 | Data

This thesis work relies on the data collected through various survey campaigns conducted in the periglacial region of Rutor Glacier.[1]

The collected data encompasses three distinct fields of study:

a. Geophysics: non-seismic methods have been widely used in recent years to estimate bathymetry and differentiate sediment types in shallow inland waters [22]. Geophysical techniques offer comprehensive coverage of the investigated area in a cost-effective manner.
   For the Seracchi Lake, ground-penetrating radar (GPR) and time domain reflectometry (TDR) techniques were employed. Geophones were also deployed in the periglacial area to detect seismic waves and provide information about bedload movements.

b. Geomatics: between 2020 and 2021, four flights were conducted over the Rutor Glacier and its periglacial area, either covering the entire area or specific portions. These surveys involved crewed aerial flights and unmanned aerial vehicle (UAV) flights using drones. The objective was to establish a unified 3D reference system and enable temporal characterization of the area by monitoring changes in the extent and morphology of the glacier surface over time [18].

c. Hydrology: to estimate both partial and total runoff in the area, four measuring stations were installed at strategic locations. The selection of these locations was based on factors such as accessibility, the shape and characteristics of watercourses or lakes, and the presence of stable rock formations or banks suitable for instrument installation [18]. Specifically, one station was positioned

[1]Some of these data have already been published and are downloadable from DataCite.

at the outlet of Santa Margherita Lake, two were located upstream of Seracchi Lake, and one was situated at the outlet of it.

Moreover, precipitation and temperature time series were used.

3.1 Geophysics data

Among the available geophysics data, this thesis specifically makes use of the depth values obtained from the post-processing of GPR (Ground-Penetrating Radar) collected data.

GPR is a non-destructive method based on the propagation of electromagnetic waves. The principle involves transmitting an electromagnetic pulse into the medium, which propagates according to the electromagnetic properties of the medium itself. When the pulse encounters a different material with distinct electromagnetic properties, a portion of the energy is reflected back and can be detected by either the transmitting antenna or a receiving one, depending on the instrumentation setup.
By analyzing the time delay between the transmitted impulse and the received signal, it is possible to estimate the depth at which has been encountered the second material. Additionally, by studying the amplitude of reflections, it is possible to differentiate between different sediment types. As a general rule, coarser sediments tend to produce higher amplitude reflected signals [23].

To estimate the distance of the target from the antenna, assuming a homogeneous medium, the two-way travel time (Twt) and the wave velocity (v) can be used:

$$Twt = 2r/v \tag{3.1}$$

The two-way travel time can be estimated by using an oscilloscope to measure the time delay between radiating the signal and detecting the reflected signal, while velocity depends on the medium.

The effectiveness of waterborne GPR in estimating bathymetry and characterizing bottom sediments depends on various factors.
Generally higher frequencies provide better resolution but shallower penetration.

The water derived from ice melting has very low conductivity and so, GPR can potentially penetrate depths of up to 25 m [23]. However, factors such as the presence of dense underwater vegetation or a high concentration of suspended sediments can introduce noise that challenges the quality of the radargrams [15] and also the type of sediment present and its reflectivity heavily influence the capability to profile the subbottom [23]. Moreover, the homogeneity hypotesis of Equation 3.1 is valid only in shallow lakes without a thermocline causing density variations and reflections before reaching the bottom layer [23].

The specific GPR survey conducted on the Rutor is dated July 10,2021 and has been performed by using a TR 200 KR GPR antenna with a central frequency of 200 MHz mounted on an inflatable rowing boat [15]. Initially, the time window for each trace was set to 600 ns, corresponding to a distance of about 10 m, but it was later increased to 1 200 ns to reach the lake's maximum depth [15]. The survey covered the entire lake area over a span of two day. The GPR profile traces are reported in Figure 3.1.

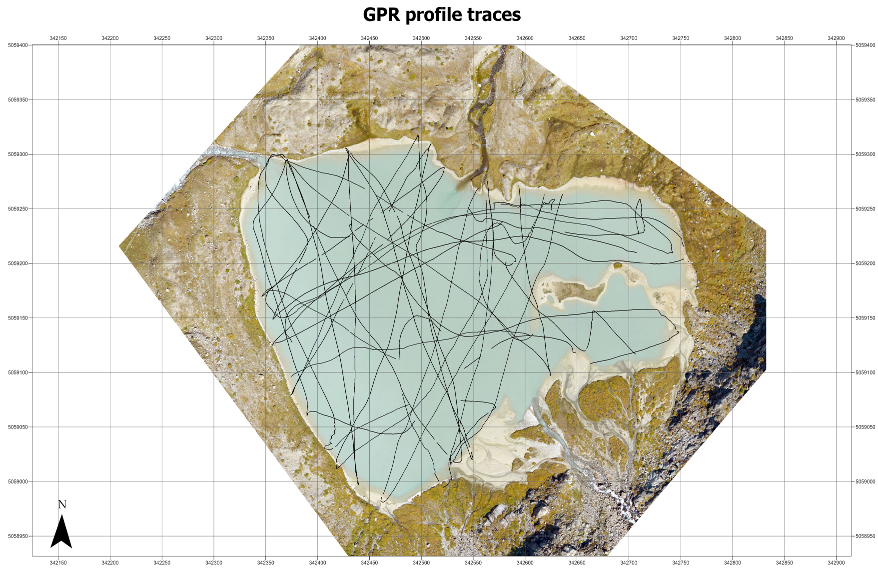

Figure 3.1: The black lines represent the boat route during the GPR acquisition in July 10, 2021.

A basic post-processing was performed on the data. The processing steps included adjusting the start time of each trace to accurately set the zero time, applying the subtract-mean filter to remove the low-frequency portion of the signal and employing the background removal filter to eliminate certain coherent instrumental noise [15].

Then, by using the average relative permittivity value obtained from TDR measurements (83.3), it was possible to calculate a propagation velocity of the GPR signals equal to 0.03287 $\mathrm{m\,ns^{-1}}$ [15] and to perform a time-to-depth conversion using Equation 3.1.

The processed GPR data resulted in sections where reflective interfaces were manually identified and picked. These sections showed two distinct interfaces: the first interface represented the bottom of the lake, while the second interface was interpreted as the bottom of the sediment layer.

In the end, the East and North coordinates, along with the corresponding depths of the picked-up points located on the lake bottom, were stored in a matrix 84 466x3.

3.2 Geomatic data

Geomatic data played a crucial role in evaluating the surface topography and providing a reference for changes in lake aspect throughout the summer season.

To achieve this, three suitable datasets were used: a drone flight on July 9, 2021, another drone flight on July 20, 2021, and an aerial flight on September 13, 2021. However, the orthophoto captured on July 9, 2021, was excluded due to snow accumulation along the lake's perimeter, which could introduce inaccuracies in determining the lake's wet perimeter. Instead, the orthophoto from July 20, 2021 was selected as the reference for the mid-summer lake conditions. Similarly, the orthophoto from September 13, 2021 was chosen as the reference for the end of the summer season. These geomatic datasets provided detailed and accurate information about the lake's surface.

Prior to the flights, 30 reference points were established using artificial markers such as squared plastered markers or crosses painted on stable rocks. These points were measured using static Global Navigation Satellite System (GNSS) and Real-Time Kinematic (RTK) positioning techniques [18]. They were strategically placed in stable areas along the glacier's moraines and rocky ridges to serve as invariant reference points for future photogrammetric flights [24]. Additionally, the IGM95 point located on the Rutor was used as a Ground Control Point (GCP) [24].

The orthophoto and respective DSM dated July 20, 2021 were generated from a drone flight, performed with a DJI Phantom 4 UAV multirotor platform equipped with a 1" RGB sensor [18]. This flight focused on surveying the proglacial lakes, covering an extent of 0.4 km^2 with an average flight height of 89.2 m and a total of 369 images captured [18].
The resulting orthophoto and DSMs have a 2D spatial resolution lower than 0.04 m, providing a highly detailed model of the area [24].

On September 13, 2021, manned photogrammetric flights were conducted by DigiSky, an EASA certified company based in Turin [24], using an ultralight aircraft equipped with a GNSS antenna and an IMU with low accuracy [24]. The camera used was a medium-format PhaseOne iXM-RS150F and multiple flights were conducted to ensure cloud-free coverage of the glacier area [18].
The flight covered an area of 34.5 km^2 at an average flight height of 877 m, capturing a total of 1 100 images [18]. The resulting orthophoto have a slightly lower spatial resolution of about 0.07 m compared to the July product, while the corresponding DSM have a spatial resolution of approximately 0.2 m [24].

All the 3D models utilize the ETRF2000/UTM32N cartographic reference system [18].

3.3 Hydrological data

In this thesis, the hydrological dynamics of the Seracchi Lake were studied using data collected at its outlet. The dataset was obtained from a self-contained water logger and transmitter (OTT ecoLog 1000) installed at the location shown in Figure 3.2.
The instrument was activated on July 10, 2021, at 11 a.m. Initially, the sampling resolution was set to half an hour, and it was later increased to 10 minutes on

July 19, 2021. The data collection period spanned from July 10, 2021, to October 14, 2021, and from May 02, 2022, to November 16, 2022. There are gaps in the data during the winter season due to the position of the instrument. During this period, the lake experiences minimal or no flow due to glaciation. As a result, the measurement point is too high relative to the water level height, leading to a lack of meaningful data during that time.

Figure 3.2: Outfall cross-section. The base orthophoto is dated July 20, 2021. The outfall cross-section points, for which elevation and position have been measured, are depicted in orange. The green point represents the position of the OTT ecoLog 1000, and the red pin indicates the rock used as reference to detect the lake water level.

The position of the instrument and the points on the bottom of the outfall cross-section were determined using a Real-Time Kinematic (RTK) positioning approach. The line of points measured along the cross-section is shown in Figure 3.2. By employing this procedure, the elevation of the bottom of the cross-section was determined to be 2 386.119 m. Additionally, the elevation of the measuring point was measured and found to be 2 386.5015 m.

By assuming the elevation of the bottom of the cross-section as the reference zero level, the water level h(t) in the cross-section results to be the hydraulic head at the reference point. Since the instrument measurements, denoted as x(t), represent the water depth expressed in meters above the measurement point, the relationship between x(t) and h(t) is:

$$h(t) = x(t) + 0.382 \tag{3.2}$$

where 0.382 m is the distance between the bottom and the measurement point. The resulting time series is shown in Figure 3.3

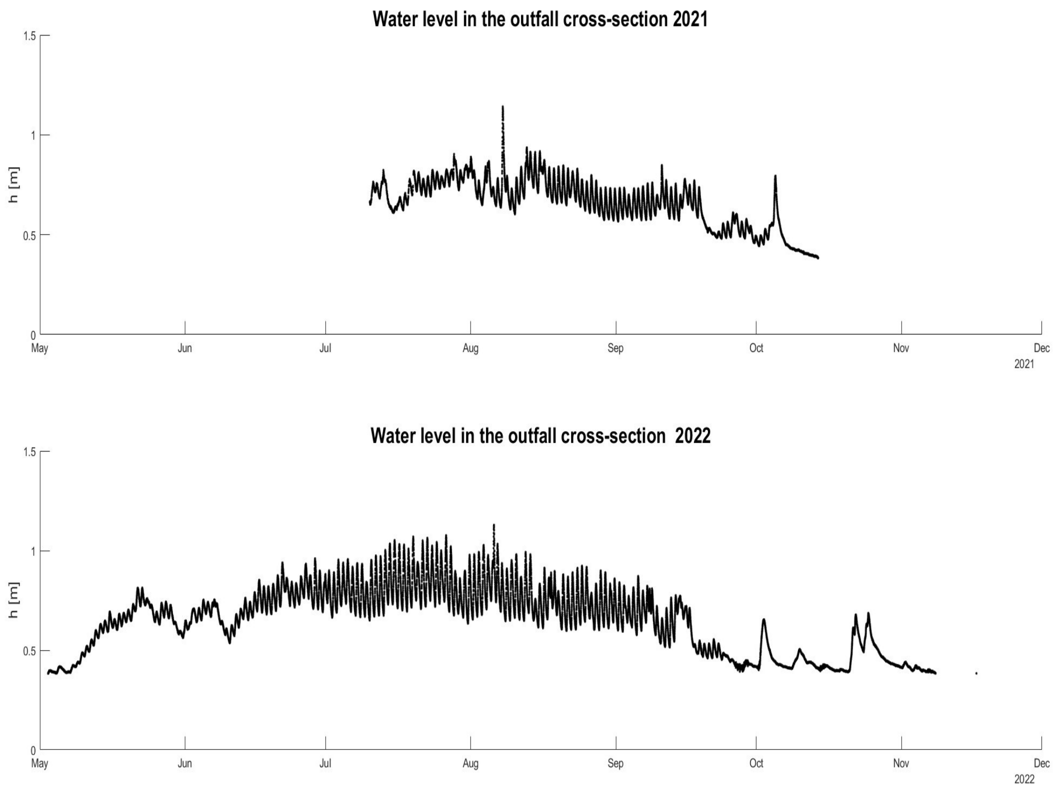

Figure 3.3: Water level h(t) on the reference point measured in the outfall cross-section.

Moreover, the hydraulic head at the reference point in the lake is not the same as the hydraulic head at the reference point in the cross-section. Given the characteristic of the downstream flow, the water level was expected to vary as schematized in Figure 3.4.
During the 2022 summer campaigns, 15 measurements were conducted to determine the difference in altitude between a rock near the lake's shore (spot height in Figure

3.2) and the water level of the lake; measurements taken by using a laser level and a leveling staff [18]. Then, by simultaneously recording the corresponding h values at each measurement time, it became possible to establish the relationship between the water level in the cross-section, h(t), and the water level in the lake, H(t). The mathematical relationship between the two variables can be expressed as:

$$H = 1.3h - 0.1279 \tag{3.3}$$

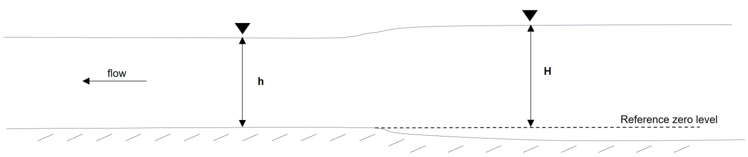

Figure 3.4: The scheme represents the expected variation in water level, given the characteristics of the downstream flow.

3.4 Climatic variables

Temperature and precipitation data were taken into consideration as external factors influencing the lake.

The values of these variables were downloaded from the ARPA VDA (Regional Environmental Protection Agency of Valle d'Aosta) website. [2] The closest meteorological station available for data collection was located at La Thuile - La Grande Tête. The station's coordinates are 5 061 212 UTM N, 337 789 UTM E, and its elevation is 2 430 m a.s.l. (Figure 3.5).

It is important to note that the meteorological station is located at a different location relative to the lake. This factor could introduce some inaccuracies in the evaluation of precipitation. For instance, recorded precipitation events may not have occurred in the exact lake area and its basin, or they may have had different intensities. Conversely, precipitation events that occurred in the lake area or its basin might not have been recorded by the meteorological station. Despite these

[2] https://presidi2.regione.vda.it/str_dataview_station/1340

potential limitations, the available meteorological data were considered a good approximation in the absence of more reliable data or clear evidence of errors.

The precipitation and temperature data on an hourly scale spanning from July 2021 to November 2022 were collected. The selected period corresponds to the time frame for which the hydrological data are accessible. The period of interest for the analysis is the summer one, meaning from June 21st to September 22nd. Therefore, the dataset was reduced and split into the two summers of 2021 and 2022. In the first case, the dataset is reduced due to the lack of hydrological data in the first 20 days.

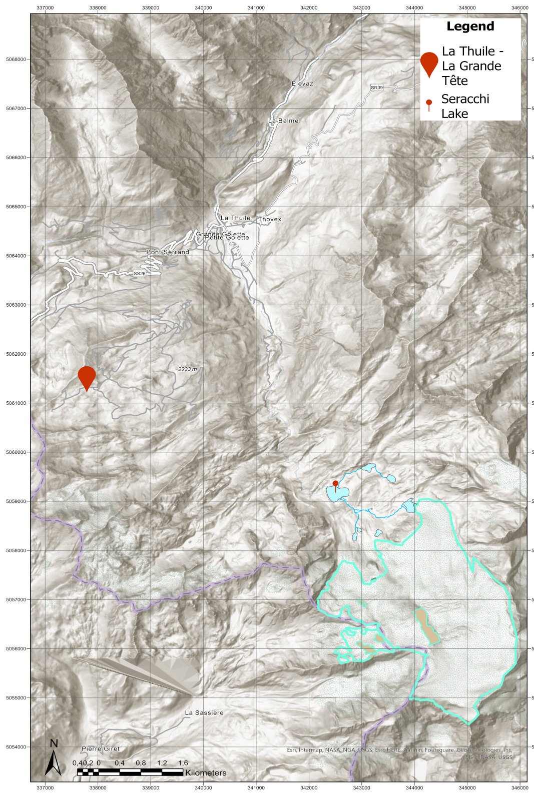

Figure 3.5: The map shows the different location between the ARPA VdA meteorological station La Thuile - La Grande Tête and the Seracchi Lake. Basemap by ESRI.

The data are plotted in Figures 3.6 and 3.7. It can be observed that there is a 2°C difference in the average seasonal temperature between the two years. Specifically, the mean temperature was 8°C in summer 2021 and 10°C in summer 2022.

Furthermore, the number of days with recorded precipitation events was significantly lower in 2022, with a total of 29 rainy days compared to the 45 observed in summer 2021.

The event with the highest intensity in 2021 was recorded on August 24 at 6:00 p.m. with an intensity of 10.2 $\mathrm{mm\,h^{-1}}$. In 2022, the maximum intensity was 6.8 $\mathrm{mm\,h^{-1}}$, and there were two events with this intensity: one on June 27 at 4:00 p.m. and the other on August 18 at 12:00 a.m..
Additionally, it is worth noting that the number of nighttime precipitation events

recorded after 8 p.m. accounted for less than 20% of the total events.

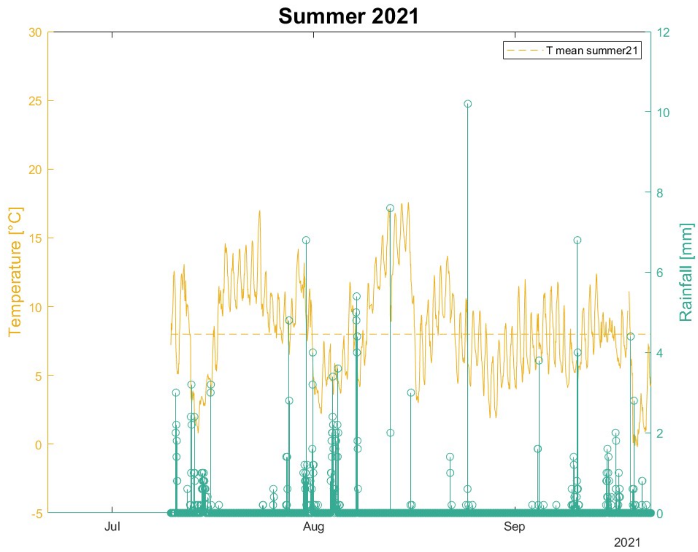

Figure 3.6: Temperature and precipitation data from July 10, 2021 to September 22, 2021.

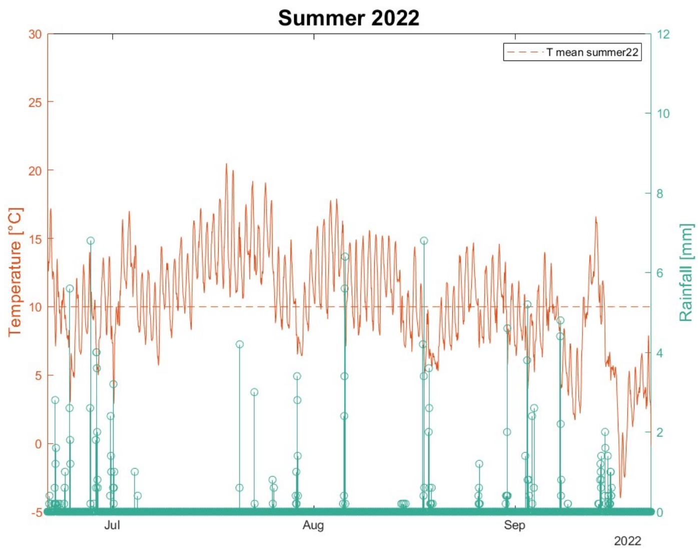

Figure 3.7: Temperature and precipitation data from June 21, 2022 to September 22, 2022.

4 | Methodology

In this chapter it will be discussed how the data were used and which kind of analysis were performed. The work can be divided into two main steps.

Firstly, it was necessary to understand the morphology of the lake. In this regard, the bathymetric reconstruction process is presented in the section 4.1. It allowed for the calculation of the lake's surface area and corresponding volume under various filling conditions, as represented by the Area-Water level and Volume-Water level curves in section 4.2.

Next, the second step concern the understanding the hydrology of the lake. To this aim, the water balance analysis was performed, as explained in section 4.3.

The results of these analysis will be discussed in the next chapter.

4.1 Bathymetry reconstruction

Bathymetry plays a crucial role in studying periglacial lakes as it provides detailed information about their morphology and depth. These lakes often exhibit features such as submerged bedrock hills, moraines, subaqueous channels, and enclosed basins [5]. Understanding the lake's bathymetry is important for geological investigations because submerged topographic barriers or sills can impact water and sediment transfer [5].

Clearly, understanding the depth and shape of the lake bottom is essential before conducting any other kind of analysis. In this section, we will present the procedure used to determine the depth of each point on the lake bottom.

The input data were the processed GPR data (section 3.1) presented as a matrix 84 466x3, where the columns represent respectively the East coordinate, the North coordinate (both in the WGS84/UTM32N coordinate system) and the depth of the measured points.

Unfortunately, the data do not cover the entire area of the lake. This limitation is due to the water level on the day of data acquisition and a technical constraint: the survey was conducted by traversing the lake by the mean of a boat carrying the GPR antenna, which only allowed data collection in areas with sufficient water depth to keep the boat afloat. It was difficult to investigate area where the water was up to 20–30 cm deep [15].
Therefore, additional data had to be gathered to fill the gaps up to the lake's full level.

Orthophotos from July 20, 2021, and September 13, 2021, were used as reference. Assuming that the lake was at its maximum capacity in July, the wet perimeter of the lake on that day was used as the zero-level reference. A GIS software was used to manually select the points along the perimeter (Figure 4.1) and their respective East and North coordinates were exported into a table. This operation required some basic assumptions regarding the border. As can be seen in the Figure 4.1, the transition between the water and the bank is not well-defined and relies solely on visual interpretation. Therefore, a general rule of thumb was applied, considering as water everything that appeared bright enough to resemble a water reflection effect. Additionally, it was necessary to determine the border between the lake and the inflows and outflows. In the the outfall cross-section the line of manually georeferenced points (Figure 3.2) was used as boarder. For the inflows, the guiding principle was to ensure that the water velocity within the lake remained as low as possible; this implied a less pronounced slope. By using the September 13, 2021 Digital Terrain Model, the contour lines were extracted, and the 2 387 m a.s.l. contour line was used as reference to mark the border. Beyond this curve, the contour lines became increasingly closer, indicating a steeper slope and higher velocity: characteristics of the stream rather than of the lake.

All points along the July perimeter were assigned a depth value of zero. To calculate the corresponding elevation value, hydrometer measurements taken during the orthophoto acquisition on July 20, 2021, were used. The x(t) series was converted to h(t) values using Equation 3.2, and further transformed into lake water level values using Equation 3.3. The transformed values were then averaged and added to the elevation of the reference level. This process resulted in a water elevation of 2 387.004 m a.s.l..

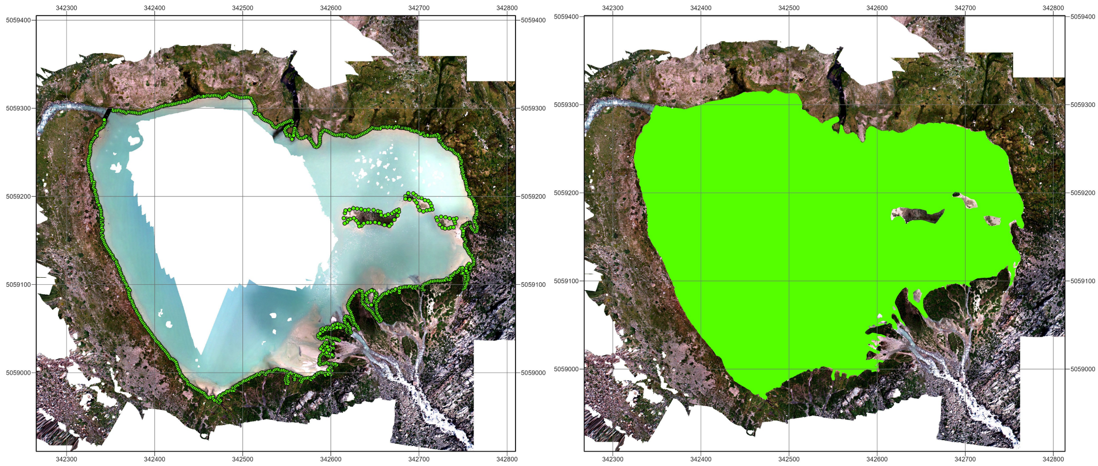

Figure 4.1: July 20,2021 lake surface perimeter and area. On the left the manually picked point belonging to the perimeter are depicted in green. These points were used as vertices to obtain the polygon representing the lake surface plotted in green on the right. It was possible to calculate the polygon area, equal to 99 354.38 m^2.

The same analysis was also conducted on the hydrometer data corresponding to the time of the September 13, 2021 orthophoto acquisition. The elevation of the lake surface was determined to be 2 386.824 m a.s.l.. This indicates that a depth below the water level equal to -0.18 m can be assigned to the points on the September wet perimeter. Similar to the July perimeter, these points were manually selected from the corresponding orthophoto (Figure 4.2) and their coordinates were exported into a table.
This additional information establishes an intermediate level between the GPR points and the zero-depth perimeter, thereby enhancing the accuracy of further analysis.

With this progress, the reconstruction of the bathymetry became possible. The aim was to interpolate all the available data points along a grid, treating the lake bottom as a flattened surface divided into discrete areas (dA) with specific East and North coordinates and depth values. The expected result of this analysis was a bathymetry matrix (mxn), where each cell corresponds to a dA and has a z value equal to or lower than zero if it belongs to the lake bottom, or NaN elsewhere.

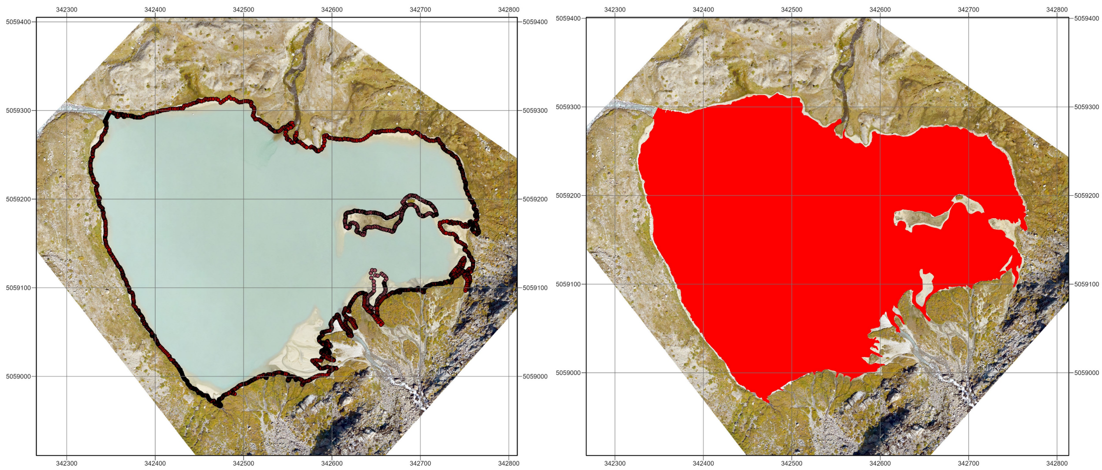

Figure 4.2: September 13,2021 lake surface perimeter and area. On the left the manually picked point belonging to the perimeter are depicted in red. These points were used as vertices to obtain the polygon representing the lake surface plotted in red on the right. It was possible to calculate the polygon area, equal to 95 240.36 m^2.

The definition of the grid was critical at this stage.
To ensure overall coherence between the available data products, the grid extension, resolution, spatial reference, and the position of cells occupied by the lake were derived from the geomatic products. The procedure is as follows:

1. The grid should be rectangular and ensure that the entire lake is covered, providing sufficient tolerance beyond its boundaries. To determine the appropriate grid extension, the September 13, 2021 orthophoto was clipped to the 2 389 m a.s.l. contour line extracted from the respective Digital Terrain Model (DTM).
   The extension of the grid was determined by the number of pixels in the resulting raster. Therefore, the grid extension matches the number of pixels in the raster, with 1 692 cells in the row direction and 2 185 cells in the column direction.

2. to determine which cell belongs to the lake, the clipped raster was masked using the September's surface area polygon. This process resulted in a grayscale georaster with pixel values ranging from 0 to 255, where 0 was associated with pixels outside the lake polygon.

3. the masked georaster contains the necessary information. The pixels represent the cells of the grid, and the coordinates of each pixel are associated with each cell. The location of the lake is known, providing the basis for the required interpolation. Thus, the masked georaster was read using MATLAB, a numerical calculation software capable of extracting the spatial reference and pixel values.

At this point, the grid has been defined, and it was possible to interpolate the GPR data and the points corresponding to the July and September perimeters along it.

There are no standard rules to follow when selecting one interpolation method over another. When dealing with spatial data, certain methods are more commonly applied than others, such as Inverse Distance Weighting (IDW) and Ordinary Kriging. These methods rely on predicting unknown values based on the proximity of known values. The main difference is that IDW employs a deterministic approach, while Kriging takes into account the spatial autocorrelation among known values [25].
Considering that the interpolation in this scenario involves variations of less than 20 cm, and lickely, a smooth surface would be sufficiently accurate, a deterministic interpolation method such as IDW could lead to valid results.
In the context of the analysis to be performed using the interpolation results, the Natural Neighbor method has been chosen. The underlying principle of Natural Neighbor interpolation is that each point has a surrounding area defined by the points that are closer to it than any other point on the surface (Voronoi polygons). Two points that share the edges of their areas are considered natural neighbors [26]. This method offers several advantages. Firstly, it is well-suited for reconstructing a surface from irregularly distributed sample points, which is the case in this scenario [26]. The definition of the neighborhood is automatic and does not rely on arbitrary conditions that do not arise naturally from the data [26]. By considering only nearby points, the interpolation produces a more accurate representation of the local surface[27]. Moreover, the interpolated heights obtained through Natural Neighbor interpolation are guaranteed to be within the range of the input samples. This ensures that trends and additional features such as peaks, pits, ridges, or

valleys are not introduced, preserving the original values and resulting in a smoother surface [26, 27].

The interpolation process was conducted in two steps. In the first step, the geophysical data and the September perimeter points (Figure 4.3) were interpolated along the grid, resulting in a matrix with the same extension, resolution, and spatial reference of the masked georaster ones. Each cell in the matrix was assigned a depth value if it fell on the lake perimeter or inside it; otherwise, the cell value was set to NaN.

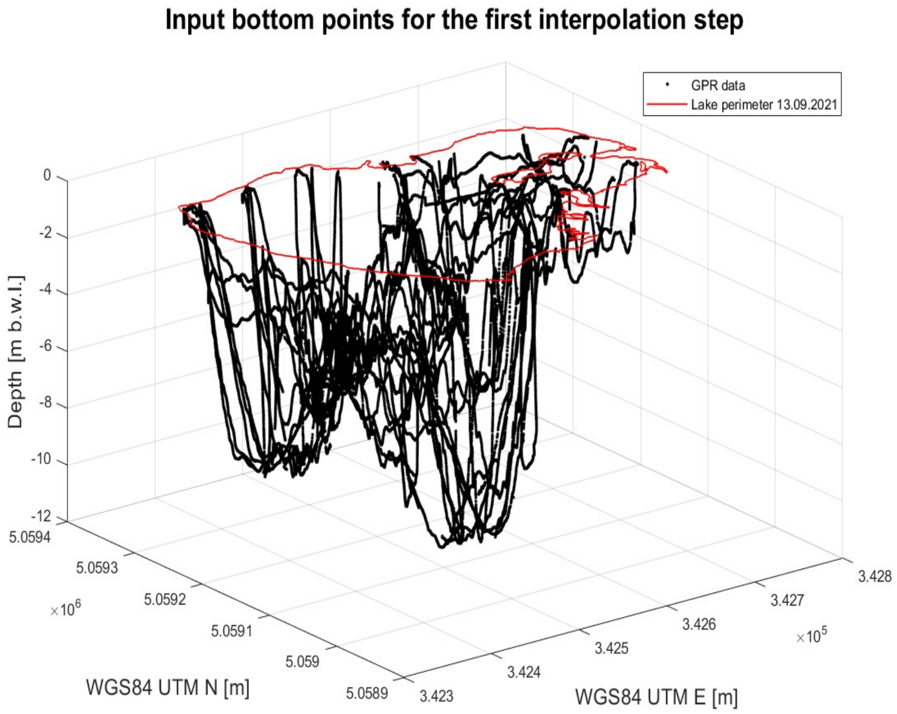

Figure 4.3: Input data for the first step interpolation consist of two datasets. The black points represent irregularly distributed sample bottom points detected using GPR (Ground Penetrating Radar) techniques. The red points correspond to the points located on the September lake surface perimeter with a depth equal to -0.18 meters. These points were identified based on the September 13, 2021 orthophoto.

In the second step, the July and September perimeter points were interpolated along a grid equal to the previous one. This step aimed to model the first 0.18 m with higher accuracy compared to directly interpolating the GPR data along with the zero-level points. The result was a matrix with with the same extension, resolution, and spatial reference of the masked georaster ones and depth values ranging from 0 to -0.18 m in the modeled area and NaN elsewhere.

Finally, the two results were merged to obtain the final bathymetry matrix, as described in section 5.1.

4.2 A-H and V-H curves production

The relationship between hydrological dynamics and the morphological characteristics of the lake was established by generating two curves: the 'Surface Area - Lake Water Level' curve (referred to as the A-H curve) and the 'Volume - Lake Water Level' curve (referred to as the V-H curve).

To create these curves, the surface area and volume values corresponding to specific water levels within the lake were required. The water level varied between 0 m, indicating an empty lake, and the maximum height of the lake, which was 10.9697 m, representing a completely full condition. The initial task was to define the surface area at each specific water level. The corresponding volumes could then be easily calculated as the sum of the individual areas at different levels.

To conduct this analysis, the available data consisted of depth values in the bathymetry matrix. For a given water level value, the surface area was determined by considering all the submerged bottom points. This was achieved by counting all the cells in the bathymetry matrix that had a depth value equal to or lower than the i-th water level. The surface area, denoted as A, was then calculated by multiplying the cell area by the number of cells, N:

$$A_{\mathrm{i}} = N \times A_{\mathrm{cells}} \tag{4.1}$$

Once the areas vector was calculated, the volumes were obtained by summing the single areas up to the i-th level:

$$V_i = \sum_{j=1}^{i} A_j \tag{4.2}$$

To model the filling dynamics, even in the case of extreme unexpected events, it was chosen to extend the analysis up to about 1.5 m above the lake's zero depth

level.
In this case, the terrain morphology was known and provided in the form of a Digital Terrain Model (DTM). From the two available DTMs, it was chosen to work with the one that has the highest resolution, corresponding to the July survey product.

The DTM was used to extract contour level curves. Its vertical resolution is approximately 0.04 m, so this interval was chosen between the curves. The first level curve was extracted at a height of 0.04 m above the lake's zero level surface, corresponding to an elevation of 2 387.044 m a.s.l.. The last level curve was extracted 1.48 m above the lake, corresponding to an elevation of 2 388.484 m a.s.l..
Regarding the lake's border, certain assumptions were made. The contour lines conform to the terrain's morphology and do not form closed lines around the lake. Therefore, in the outflow zone, a closing section needed to be determined. Initially, the georeferenced points in the outfall cross-section were extended and used to close the contours. However, this approach had the potential to exclude portions of land that belong to the lake's banks. As a result, it was decided to close the contour lines just before the stream flow starts to accelerate.
The closed curves obtained represent the wet perimeter based on the elevation, enabling the calculation of the enclosed area.

In Figure 4.1, it can be observed that even when the lake reaches its maximum capacity, there are portions of land within it that remain uncovered. Therefore, when modeling the area above the lake, it is necessary to consider these small islands. The contour lines with 0.04 m spacing were extracted, and their enclosed areas were calculated. It was observed that these islands contribute to the i-th area for the first 0.7626 meters above the lake's zero depth level.

In the end, the i-th surface areas, given the height, were obtained as follows:

$$A_{\mathrm{i}}^{\mathrm{up}} = \mathrm{A}_{\mathrm{zero\ level}} + \sum_{j=1}^{i} A_{\mathrm{j}}^{\mathrm{island}} + \sum_{j=1}^{i} A_{\mathrm{j}}^{\mathrm{contour}} \tag{4.3}$$

Consequently, the enclosed volumes given the i-th level were obtained as sum of the single areas.

The resulting curves are presented in the section 5.2.

4.2.1 Curves interpolation

The empirical data collected using the methodology described thus far needs to be translated into an analytical function. For the sake of further analysis, the modeling can be focused on the section of the contour curves that corresponds to the water level allowing the outflow to occur, specifically above the bottom of the outfall cross-section, located at an elevation of 2 386.119 m a.s.l.. From this point onwards, this reference level will be assumed as the zero reference level, meaning both h and H are set to zero at this point.
The experimental curves of areas and volumes as functions of the lake water level for $H \geq 0$, as shown in the Figure 4.4.

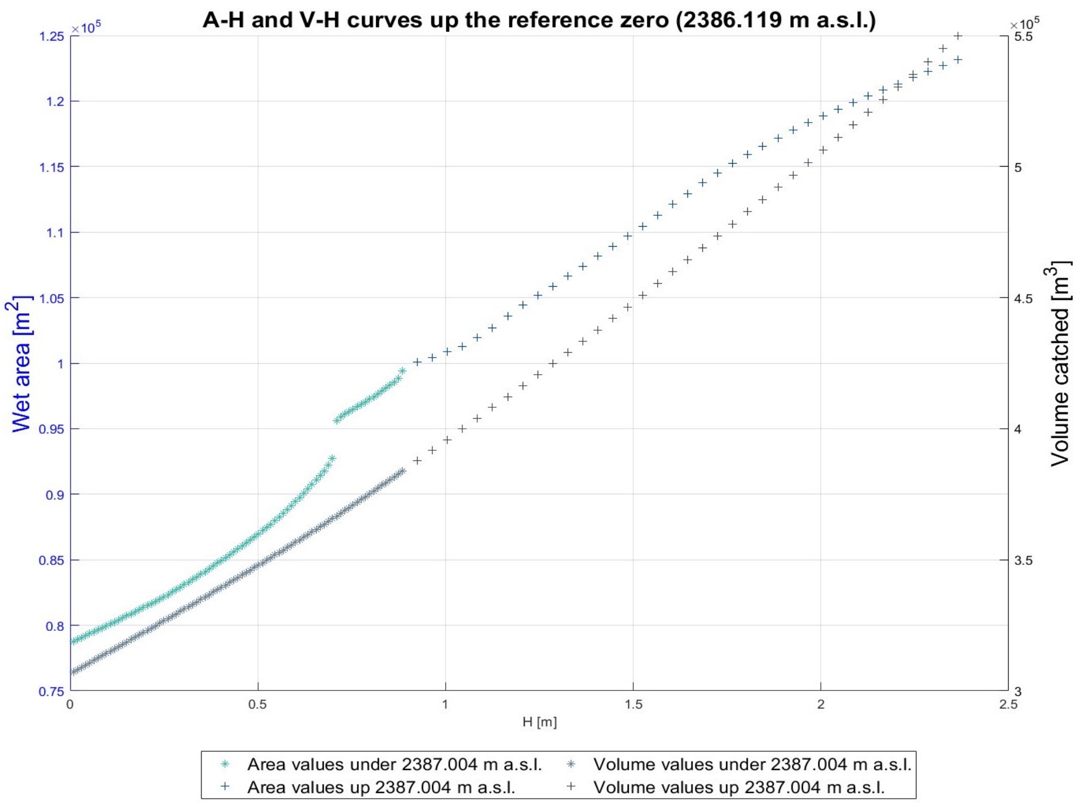

Figure 4.4: The A-H and V-H empirical curves represent the relationship between the height (H) of the water surface with respect to the reference zero level and the corresponding area (A) and volume (V) of the lake. The reference zero level (z) is equal to 2386.119 m.

The underlying hypothesis for the analysis is that V(H) represents the integral of A(H), and vice versa, A(H) must be equal to the derivative of V(H).
Initially, attempts were made to model both curves using polynomial functions, with f(x) representing V(H) and f'(x) representing A(H). A system of linear equations was set up to find the parameters that satisfy this condition, but no solution was found.
Therefore, it was decided to begin the modeling by analyzing the A-H curve, which exhibits more irregularities. In particular, the curve shows regular growth until $H = 0.709711$ m, where a vertical jump is observed. Between the surface area at the $H = 0.709711$ m level and the one at the previous level there is a greater expansion of the area for a small increment in height. This behavior is likely artificial and a result of the interpolation process.
Subsequently, the curve continues to increase until $H = 0.874$ m, where another very small vertical jump in the curve is observed.
Beyond this point, the curve continues to grow, but at a slower pace compared to before. This last segment corresponds to the part above the July free surface, where the contour lines are more widely spaced and often follow the vegetation or rocks, resulting in small area increments as H varies.

Given the observed behavior, it was decided to divide the curve fitting into two segments: the first segment ranging from $H = 0$ m to $H \leq 0.709711$ m and the second segment valid for $H > 0.709711$ m.

- $H \leq 0.709711$ m:
  For the H values in question, the empirical A-H curve segment demonstrates undisturbed growth, indicating that a fitting equation representing unlimited growth is appropriate. The objective was to find a function that fits the data well and whose integral also aligns with the empirical volume data.
  Similarly, the empirical volume curve segment also exhibits undisturbed growth. This suggests that both the derivative and the integral functions shall grow at a similar pace, indicating that an exponential function is suitable for representing the data.
  To perform the fitting process, the "curve fitting" tool in MATLAB was employed. The interpolation equation was customized to effectively capture

the exponential growth pattern exhibited by the curves.

The A-H empirical data were interpolated by using the following equation:

$$f'(x) = a \cdot b \cdot e^{bx} + c \tag{4.4}$$

From the fitting it results that with a 95% confidence interval the parameters values are:

- a = 4.938,
- b = 1.494,
- c = 7.143e+04.

To assess the goodness of the fit the coefficient of determination was calculated. It provides an estimate of the proportion of variation in the response variable that can be explained by the model. The value of the coefficient of determination can range from 0 to 1. A value of 1 indicates that the model perfectly explains the variation in the data, meaning that all points lie on the regression line. A value of 0 indicates that the model does not explain any variation in the data, and all points are far from the regression line. In this case the determination coefficient was calculated to be $R^2 = 0.996$, indicating a good fit of the model to the data. This high value suggests that approximately 99.6% of the variation in the response variable can be explained by the regression model.

Subsequently, the integral of equation 4.4 was applied to interpolate the V-H empirical curve:

$$f(x) = a \cdot e^{bx} + c \cdot x + d \tag{4.5}$$

The parameter values that yield a 95% confidence interval are as follows:

- a = 5.271,
- b = 1.456,
- c = 7.117e+04,
- d = 3.013e+05.

Also in this case the coefficient of determination was $R^2 = 0.996$.
Therefore, both models yield satisfactory results, although there is a slight variation in the estimated parameters. To obtain a unique solution, the parameters a, b, and c resulting from the two fittings were averaged.

- $H > 0.709711$ m:
  The empirical A-H curve segment exhibits a behavior that resembles growth limited by an upper bound, such as the maximum elevation of the terrain. Therefore, an attempt was made to model this segment with a logistic equation. However, it was found that although this model approximates the experimental areas data very well, its integral does not accurately reproduce the volume data.
  As a result, a simple linear interpolation function was chosen, such that:

$$f(x) = a_0 + a_1 \cdot x + \frac{a_2}{2} \cdot x^2 + \frac{a_3}{3} \cdot x^3 \tag{4.6}$$

$$f'(x) = a_1 + a_2 \cdot x + a_3 \cdot x^2 \tag{4.7}$$

To determine the best set of parameters, a system of equations was set up using the derivative values as constraints. This system was given by:

$$A \cdot a = y \tag{4.8}$$

$$\begin{bmatrix} 1 & H_1 & \frac{1}{2}H_1^2 & \frac{1}{2}H_1^3 \\ \vdots & \vdots & \vdots & \vdots \\ 1 & H_{\mu_1} & \frac{1}{3}H_{\mu_1}^2 & \frac{1}{3}H_{\mu_1}^3 \\ 0 & 1 & H_1 & H_1^2 \\ \vdots & \vdots & \vdots & \vdots \\ 0 & 1 & H_{\mu_2} & H_{\mu_2}^2 \end{bmatrix} \begin{bmatrix} a_0 & & & \\ \vdots & \vdots & \ddots & \vdots \\ a_4 & & & \end{bmatrix} = \begin{bmatrix} y_1 \\ \vdots \\ y_{\mu_1} \\ y'_1 \\ \vdots \\ y'_{\mu_2} \end{bmatrix} \tag{4.9}$$

A is the measurement location matrix, where x have been substituted with the H values, a is the parameter matrix, and y is the measurements matrix. The measurements matrix is obtained by concatenating the μ_1 empirical volume values and the μ_2 empirical area values.

The linsolve function in MATLAB was used to solve this system of equations. It decomposes the matrix A into an orthogonal matrix Q and an upper triangular matrix R. The parameter matrix is then obtained as:

$$a = R^{-1} \cdot (Q^T \cdot y) \tag{4.10}$$

The resulting parameter values are:

- a0 = -1.8180e+03,
- a1 = 2.2784e+04,
- a2 = 8.0185e+04,
- a3 = 3.0436e+05.

The interpolated values of the areas and volumes were calculated for different values of H. The results are shown in section 5.2.

4.3 Mass Balance

The reconstructed bathymetry made it clear that the Seracchi Lake is a shallow lake. This limited depth exposes the lake to be highly responsive to fluctuations in water levels. To gain a more comprehensive understanding of the lake's hydrodynamics, a water balance analysis was conducted. This analysis aims to assess the overall water dynamics within the lake and investigate its response to changing conditions.

The fundamental principle of a water balance analysis is based on the conservation of mass, where the sum of the inflows minus the sum of the outflows should equal the rate of change of volume over time. The analysis involves quantifying the various inputs and outputs of water in the lake system.

Typically, the input fluxes considered in a water balance analysis include direct precipitation, surface runoff, and stream inflow. On the other hand, the output fluxes consist of evapotranspiration and stream outflow. Other factors influencing the water level and volume of the lake could be groundwater fluxes and, given the location, the snow drift [28]. However, obtaining all of this information can be challenging. For example, accurately evaluating terms such as snow drift and evapotranspiration requires specific data collected directly from the area of interest.

In the specific case of this thesis, certain simplifications were necessary due to limitations in the available data. Referring to the hydrogeological cartography of the Aosta Valley region, it was assumed that there is negligible groundwater recharge in the area surrounding the lake. Moreover, due to the lack of sufficient data, the estimation of precipitation and evapotranspiration terms was not possible. However, given the size of the lake, it is reasonable to approximate that the contribution of precipitation and evapotranspiration is relatively small and can be neglected without significantly affecting the results.
Therefore, a simplified equation was adopted for the water balance analysis, in the form of:

$$Q_{\mathrm{IN}} - Q_{\mathrm{OUT}} = \frac{dV}{dt} \tag{4.11}$$

The unknown term in this equation is the inflow discharge, represented by Q_{IN}. In this case, the inflows consist of the combined contributions from two tributaries and potential runoff, while the direct precipitation term has been neglected. Unfortunately, due to limitations in installing instruments and directly measuring these individual contributions, it was not possible to separate the Q_{IN} value into its constituent parts. Therefore, the total inflow discharge was considered as a single value.
On the other hand, the outflow discharge, represented by Q_{OUT}, is solely determined by the outfall stream, as the effects of evapotranspiration have been neglected in this analysis. The Q_{OUT} value was determined using available data, such as the rate of change of volume ($\frac{dV}{dt}$).

The outflow occurs when the water level on the reference point in the outfall cross-section is greater than 0 m. The relationship between the h and the outflow discharge has been derived by the CC-Glacier Lab working group and has been provided:

- for $h \geq 0.49$ m, the relationship is given analytically as:

$$Q_{\mathrm{OUT}} = 12.118 \cdot h^{4.0042} \tag{4.12}$$

- for $0 \leq h < 0.49$ m, the outflow values are tabulated on a point-by-point basis. This means that for every 1 mm increase in h, a corresponding value of Q is provided.

Thus, the primary data for the analysis consisted of the time series of water level at the outfall cross-section h(t) on a 10 minutes scale, reported in Figure 3.3. The outflow discharge time series, $Q_{\text{OUT}}(t)$ was then reconstructed by applying Equation 4.12 for h(t) values greater than or equal to 0.49 m and by using the tabulated values for h(t) values less than 0.49 m. The resulting $Q_{\text{OUT}}(t)$ values are expressed in $\text{m}^3\,\text{s}^{-1}$ and plotted in Figure 4.5.

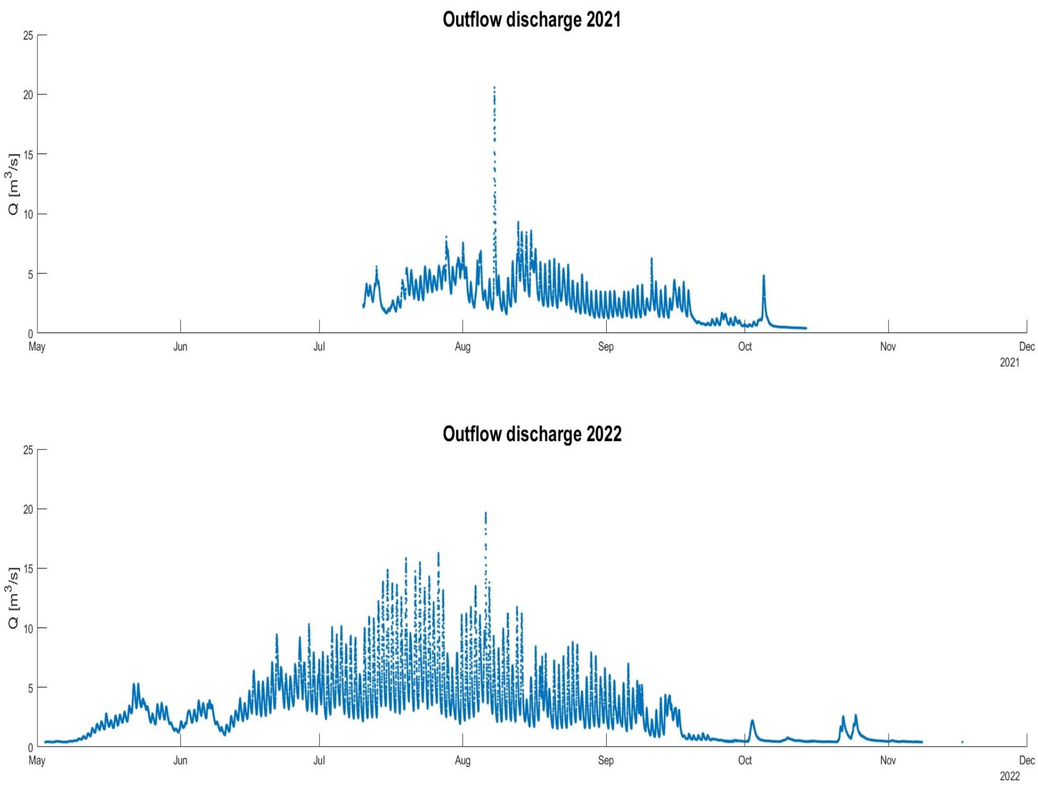

Figure 4.5: Outflow Discharge ($Q_{\text{OUT}}(t)$) as a function of Water Level (h) in the Seracchi Lake. The upper graph shows the relationship between the water level and the corresponding outflow discharge values for h values recorded during the 2021. The belower graph shows the relationship between the water level and the corresponding outflow discharge values for h values recorded during the 2022.

The term $\frac{dV}{dt}$ can be rewritten as:

$$\frac{d[V(H(t))]}{dt} = \frac{dV(H)}{dH} \cdot \frac{dH(t)}{dt} \tag{4.13}$$

The first factor $\frac{dV(H)}{dH}$ represents the derivative of the volume with respect to the lake water level. It is exactly A(H), which analytical function has been calculated and can be found in Equation 5.1 and Equation 5.2.

Regarding the second factor, the time series of water level in the lake with respect to the reference point, H(t), was obtained from h(t) by applying equation 3.3. However, it was observed that the h(t) series exhibited rapid fluctuations, leading to unrealistic oscillations in the lake water level values.
To address this issue, a moving average technique was applied to the H(t) series. The choice of the moving average window was crucial. The purpose of the moving average is to smooth out oscillations with a period equal to the number of terms included in the mean calculation. Thus, selecting a window that is too small may not effectively capture the oscillations, while a window that is too large could excessively smooth the data. As a compromise, a window period of 1 hour was considered appropriate. Given that the values are recorded every 10 minutes, the number of terms included in the mean calculation was k=7 (representing 1 hour). The resulting time series is depicted in Figure 4.6.
With the obtained results, it was possible to calculate the derivative term $\frac{dH(t)}{dt}$.

Finally, the term $\frac{d[V(H(t))]}{dt}$ was calculated by multiplying the two series and adding to it the $Q_{\mathrm{OUT}}(t)$, the $Q_{\mathrm{IN}}(t)$ values were obtained.

Results are presented in the section 5.3.

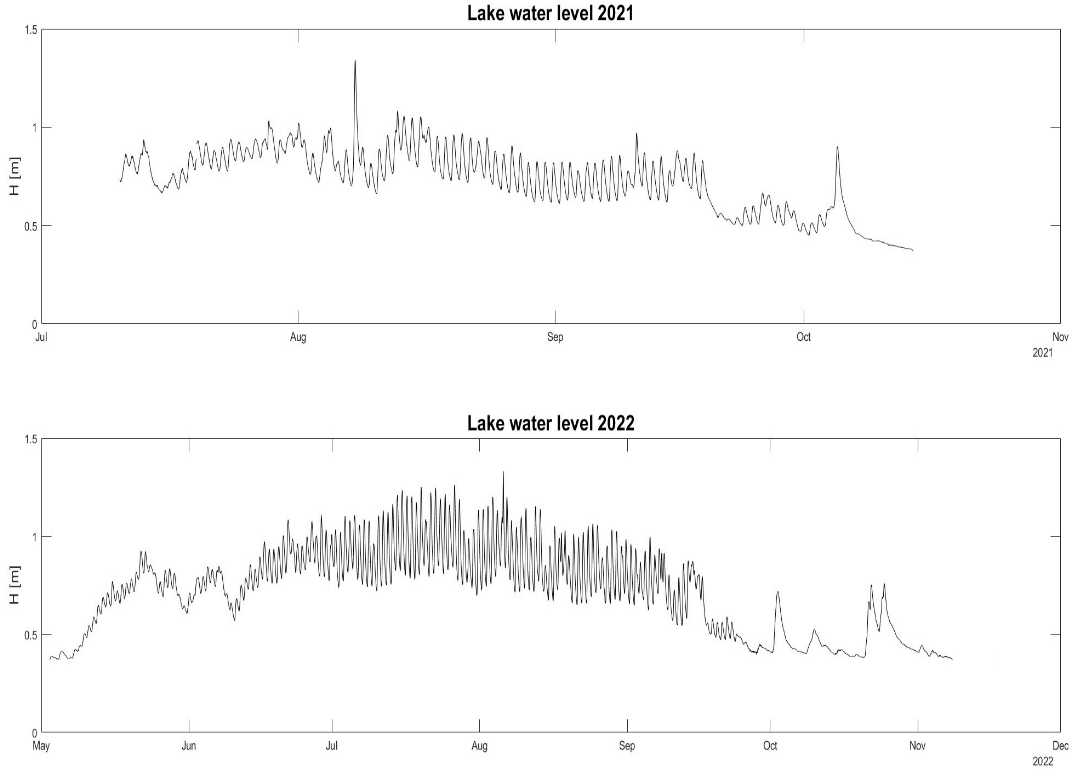

Figure 4.6: The graph illustrates the variation of the water level in Seracchi Lake, H, over time. The upper graph refers to 2021, the lower to 2022.

5 | Results

In this chapter the results of the previous analysis (chapter 4) will be presented and discussed.

5.1 Bathymetry reconstruction

As explained in section 4.1, the grid interpolation of the sample points obtained from GPR processing and the July and September 2021 orthophotos was performed in two steps.

From the first interpolation step, a 1 692x2 185 matrix was generated. Each cell in the matrix represents the depth of the lake's bottom points between the lowest point at a depth of 10.9697 m and the free surface on September 13, 2021, which is 0.18 m deeper than the lake's free surface under full filling conditions.
The resulting surface extends in terms of elevation from 2 376.0343 m a.s.l. to 2 386.824 m a.s.l. and is plotted in Figure 5.1.

Cells outside the lake area should be assigned a NaN value. However, as observed in Figure 5.1, the interpolated surface extends beyond the perimeter boundary. To correct this issue, the matrix was adjusted by assigning NaN values to the cells not belonging to the lake. The position of those cells indexes was obtained from the masked orthophoto, by finding the index of the pixels with assigned 0 value. The resulting surface, after correction, is displayed in Figure 5.2.

The second step of interpolation, conducted between the -0.18 m depth level and the zero level, yielded a 1 692x2 185 matrix with the depth values assigned to the cells within the first 18 cm, while NaN values were assigned elsewhere. The resulting surface is shown in Figure 5.3. Similar to the previous step, inaccuracies were observed regarding the perimeter boundary. To address this issue, the same correction process was applied to the interpolated grid.

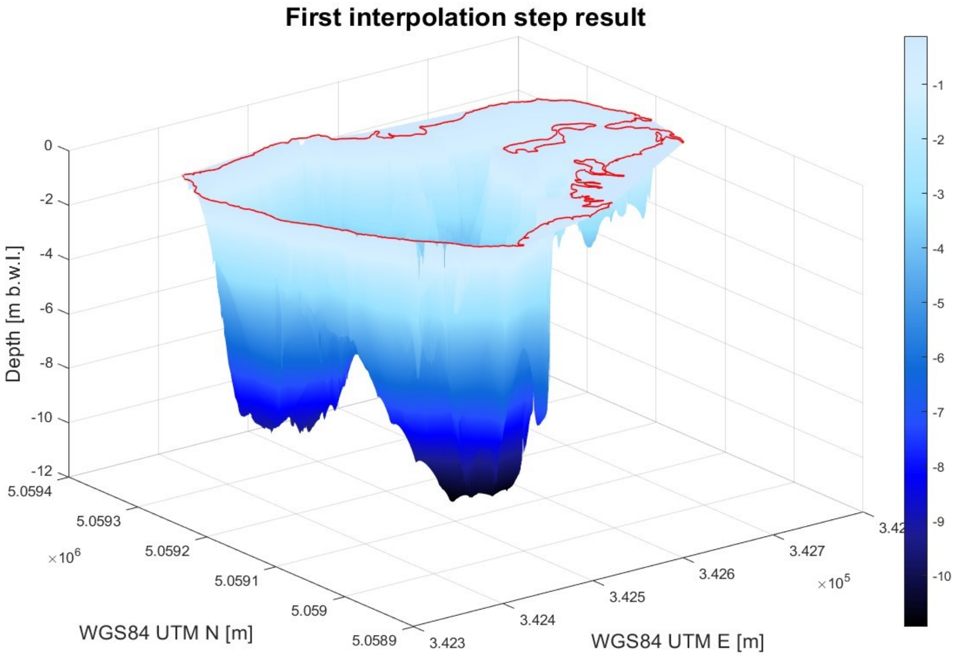

Figure 5.1: The Seracchi Lake interpolated bathymetry surface extending from an elevation of 2 376.0343 m a.s.l. to 2 386.824 m a.s.l.. In red the lake perimeter when the water level height is 2 386.824 m a.s.l..

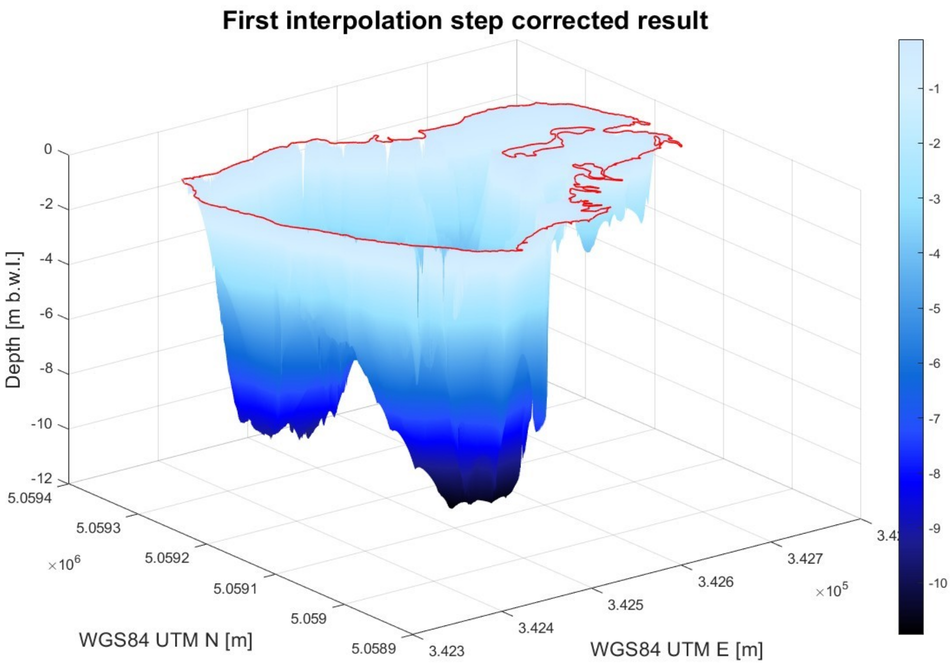

Figure 5.2: The corrected Seracchi Lake bathymetry extending from an elevation of 2 376.0343 m a.s.l. to 2 386.824 m a.s.l., after assigning NaN values to the cells outside the lake area.

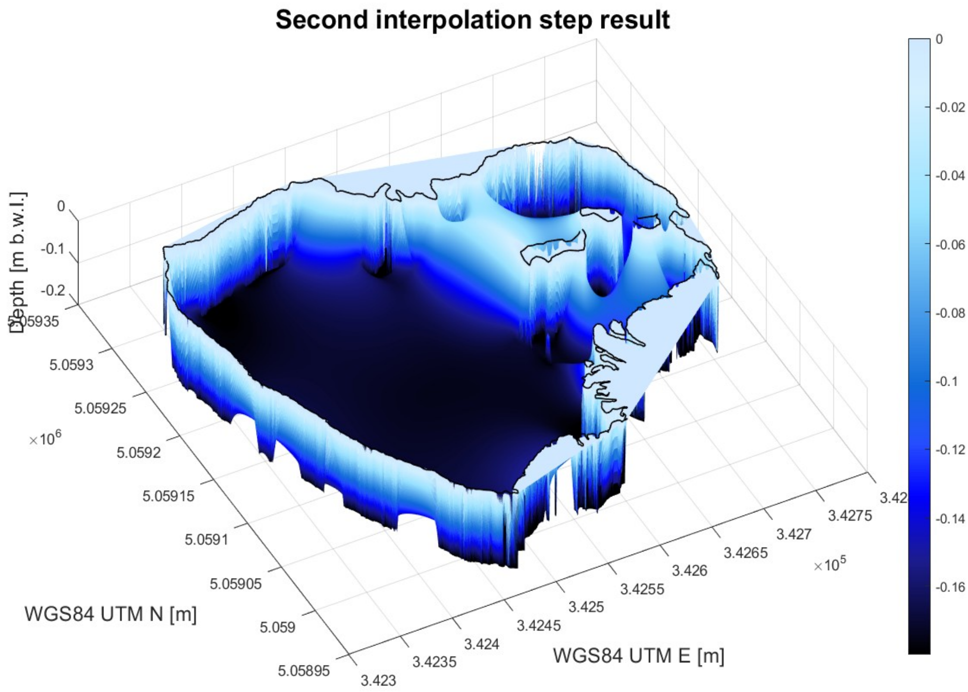

Figure 5.3: The interpolated bathymetry surface of Seracchi Lake extending from an elevation of 2 386.824 m a.s.l. to 2 387.004 m a.s.l. It is the result of the second step of interpolation.

Finally, the two matrices resulting from the interpolation steps were merged to obtain the final bathymetry matrix. To ensure accuracy during the merging phase, a test was conducted by comparing the indexes of cells corresponding to the surface area at the 0 m level and the -0.18 m depth level with the corresponding pixels in the masked georasters. The test yielded positive results, confirming the successful merging process.

The batymetry matrix has 1 692 cells in the row direction and 2 185 cells in the column direction. The cell in the lower left corner has coordinates of 3.4223e+05 UTM E and 5.0589e+06 UTM N. The spatial resolution is 0.25 m, meaning that each cell corresponds to an area of $A_{cells} = 0.0625\text{m}^2$.

From the analysis, it can be concluded that Seracchi Lake extends from 2 376.0343 m a.s.l. to 2 387.004 m a.s.l.. As depicted in Figure 5.4, the bathymetry exhibits two main cones in the western part, with the southern cone reaching the deepest point. The eastern part of the lake features a shallower and more irregular bottom, influenced by glacial meltwater (and its suspended material) that forms irregular deltas. In the middle of the lake, there is a tongue of land that reaches higher elevations than 2 387.004 m a.s.l., causing the formation of small islands when the lake is at its maximum filling conditions.

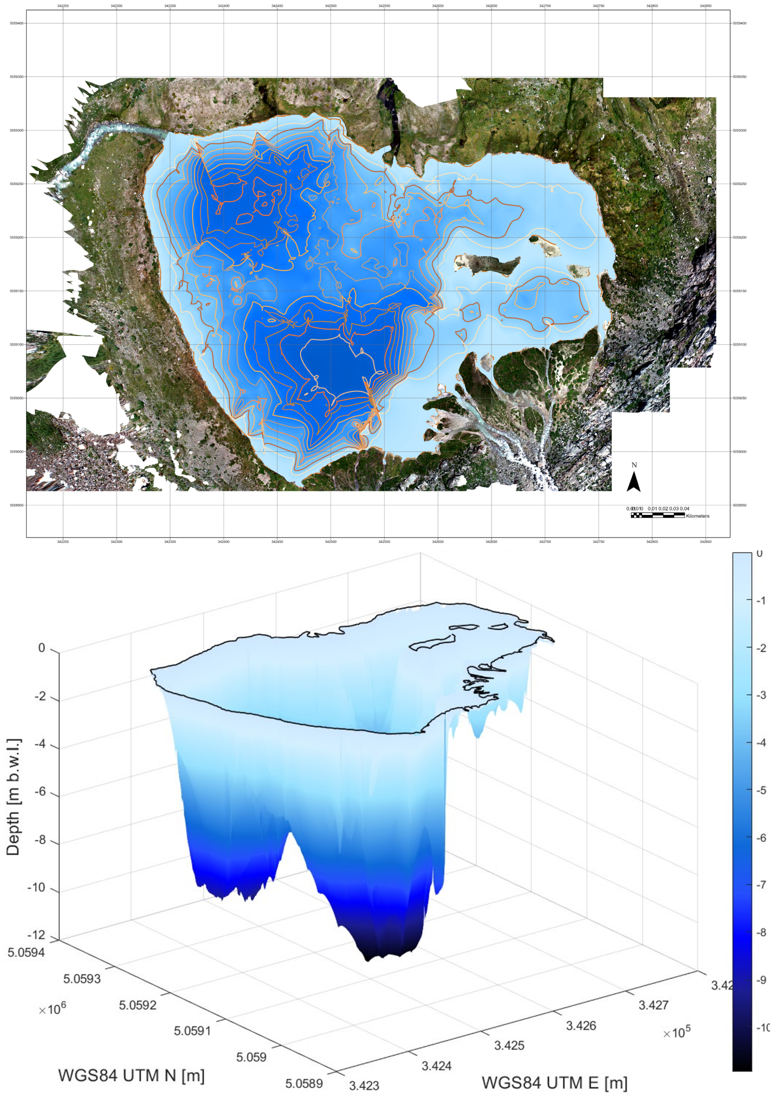

Figure 5.4: Seracchi Lake bathymetry. The upper part of the image displays the contour lines representing the bathymetry of Seracchi Lake, with an interval of 1 meter. These lines provide a detailed representation of the lake's underwater topography, illustrating the variations in depth throughout the basin. The lower part of the image depicts the resulting surface, which spans from an elevation of 2 376.0343 m a.s.l. to 2 387.004 m a.s.l..

5.2 A-H and V-H curves production

The A-H and V-H curves illustrate the relationship between the area (A) and volume (V) of the lake and the water level (H) within the lake. The results are based on two subsets of empirical data plotted in Figure 5.5.

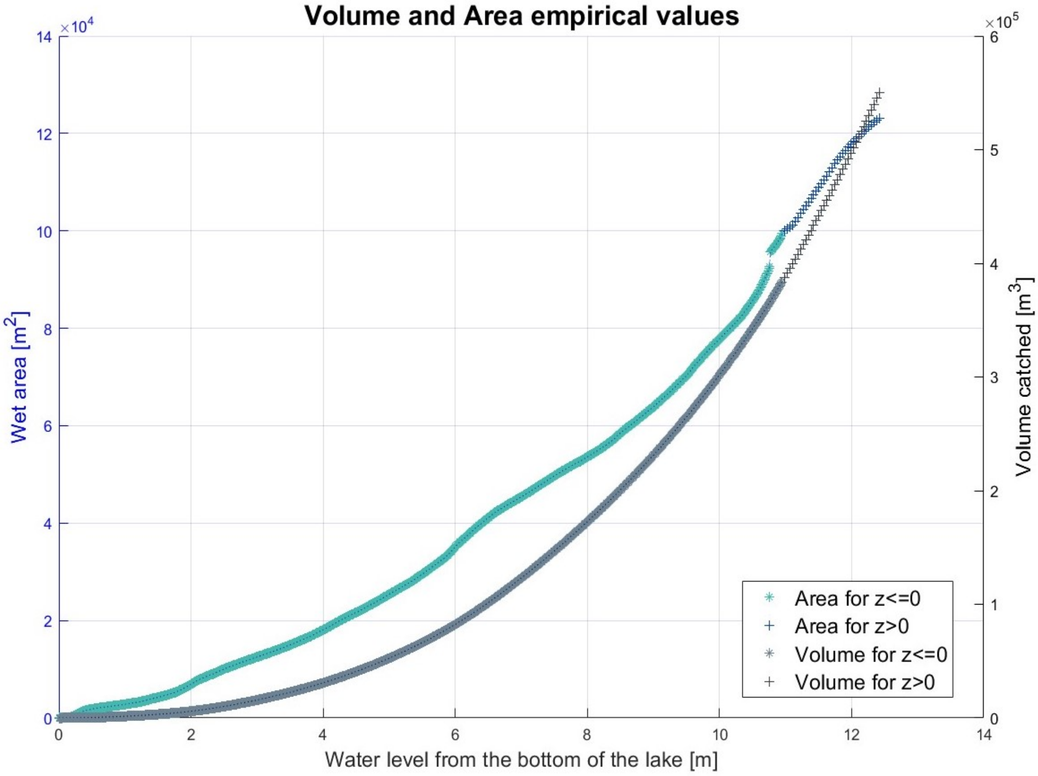

Figure 5.5: Empirical values of the lake's area (A) and volume (V). The x-axis represents the water level in m, ranging from the bottom of the lake to the 1.5 m up to the full filling conditions. The z=0 free surface corresponds to the water level equal to 10.9697 m.

The first subset, consists of the area and volume vectors calculated using Equation 4.1 and 4.2. The values are computed relative to the water level measured from the bottom of the lake. Thus, the first value was evaluated at the bottom of the lake. It corresponds to a water level equal to zero, representing empty conditions. The last value was evaluated at the zero depth level. It corresponds to a water level equal to 10.9697 m, representing full filling conditions.

The second subset regards the 1.5 m up the lake free surface. Also in this case the area and volumes values have been calculated with respect to the lake water level measured from the bottom of the lake.

To fit the curves, the x-axis was transformed into lake water levels relative to the reference zero level (2386.119 m) and the dataset was reduced only to points from this reference level up (see Figure 4.4). The curve fitting process was performed by using piecewise functions, returning the analytical Equations 5.1 and 5.2. As explained in section 4.2, this approach allows for capturing the change in pace observed in the empirical area series.

The parameters describing the A(H) and V(H) functions for the range $0 \leq H \leq 0.709711$ m were determined by averaging the parameters obtained from the two separate curve fittings performed on the empirical data. To evaluate the goodness of the overall fit, the coefficient of determination (R^2) was calculated. The results are highly satisfactory, with a R^2 value of 0.996 for the areas and 1 for the volumes. These values indicate a strong fit between the model and the empirical data.

The resulting curves, as shown in Figure 5.6, effectively capture the real behavior of the lake. The volume continues to increase steadily, indicating a progressive accumulation of water as the water level rises. On the other hand, the area exhibits an increasing trend with changing pace. This behavior is due to the natural boundaries imposed by the surface topography, which limit the expansion of the lake's surface area. As the water level increases, the area growth gradually slows down and eventually reaches a maximum value.

$$A(H) = \begin{cases} 5\,104.5 \cdot 1.475 \cdot e^{1.475H} + 71\,300 & \text{for } 0 \leq H \leq 0.709711 \\ -1\,818.02 \cdot H^2 + 22\,783.9 \cdot H + 80\,184.61 & \text{for } H > 0.709711 \end{cases} \tag{5.1}$$

$$V(H) = \begin{cases} 5\,104.5 \cdot e^{1.475H} + 71\,300H + 301\,300 & \text{for } 0 \leq H \leq 0.709711 \\ -\frac{1\,818.02}{3} \cdot H^3 + \frac{22\,783.9}{2} \cdot H^2 + 80\,184.61 \cdot H + 3\,045\,357.27 & \text{for } H > 0.709711 \end{cases} \tag{5.2}$$

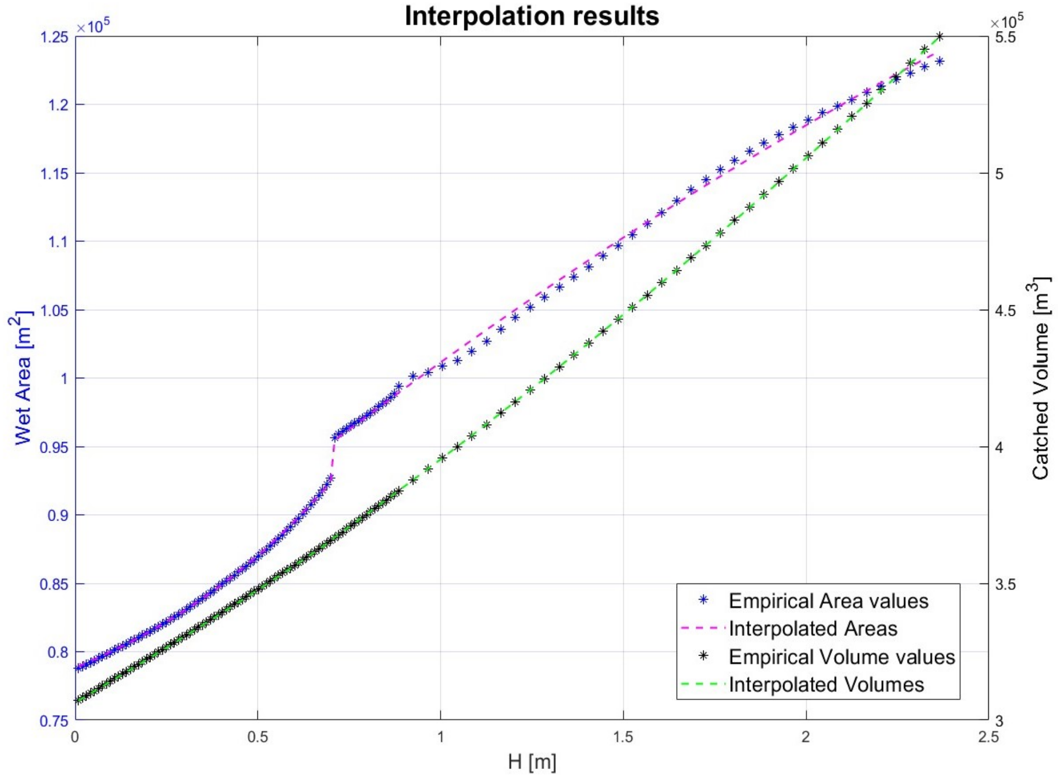

Figure 5.6: The interpolated curves for the lake's area (A) and volume (V) with respect to the water level H. The x-axis represents the lake water level in m with respect to the reference zero level (2386.119 m a.s.l.). The value $H = 0.8850$ m corresponds to z=0 free surface.

The surface area corresponding to July filling conditions was calculating by applying Equation 5.1. It amounts to 99 403.47 m^2. To ensure the coherence of the data, a comparison was made between the calculated value and the geometrically obtained value from the polygon area in Figure 4.1. The first one is slightly higher (by approximately 10 m^2). However, this small discrepancy is expected due to the method of calculation used (Equatoin 4.1), which assumes that the lake precisely follows the shape of the cells, leading to a slight overestimation of the area. Considering the inherent irregularity of the lake boundary, this small difference is considered acceptable.

Once the reliability of the fitted curves in estimating the area and volume of the lake at different water levels has been demonstrated, it becomes possible to quantify the maximum volume of the lake, equal to 549 915.29 m^3.

5.3 Mass Balance

The mass balance analysis serves two important purposes in this thesis work. Firstly, it enables the estimation of the inflow time series. Obtaining a reliable dataset of calculated inflows (Q_{IN}) is one of the most valuable outcomes of this study. Direct measurements of Q_{IN} were unavailable due to safety considerations that prevented the installation of instruments for direct water level measurements or the reconstruction of the inflow cross-section.
According to the hypothesis underlying the analysis, the calculated Seracchi Lake inflows is made up by three single contributors. Therea are two main sources: one from the northeastern side of the lake, originating from Santa Margherita lake, and the other, likely the most significant contribution, on the southern side of the lake originating from the glacier. Additionally, during precipitation events, there is runoff contributing to the inflows.

The mass balance analysis is also an essential tool for comprehending the hydrological dynamics of the lake. It allows for a comprehensive investigation of the complex interactions between precipitation, runoff, and storage within the lake system. Valuable insights can be gained regarding various aspects, such as the lake's response to rainfall events, the contribution of glacial meltwater, and its seasonal and interannual variations or the lake's role in capturing and regulating the flow of glacial meltwater.

Figure 5.7 illustrates the inflow (Q_{IN}) and outflow (Q_{OUT}) terms resulting from the mass balance. The dataset obtained has a resolution of one value every 10 minutes, corresponding to the sampling period of the input data. If needed, these data can be resampled to higher time scales to meet specific requirements.

During the summer of 2021, the lake experienced discharge values ranging from 0 to 10 $m^3\,s^{-1}$, with one exceptional event on August 7th at 20:10 when the inflow (Q_{IN}) reached 21.8 $m^3\,s^{-1}$. In contrast, the summer of 2022 exhibited a significant increase in discharge values, nearly five times higher than the previous year. Discharges ranged from 0 to 15 $m^3\,s^{-1}$, with the highest value recorded

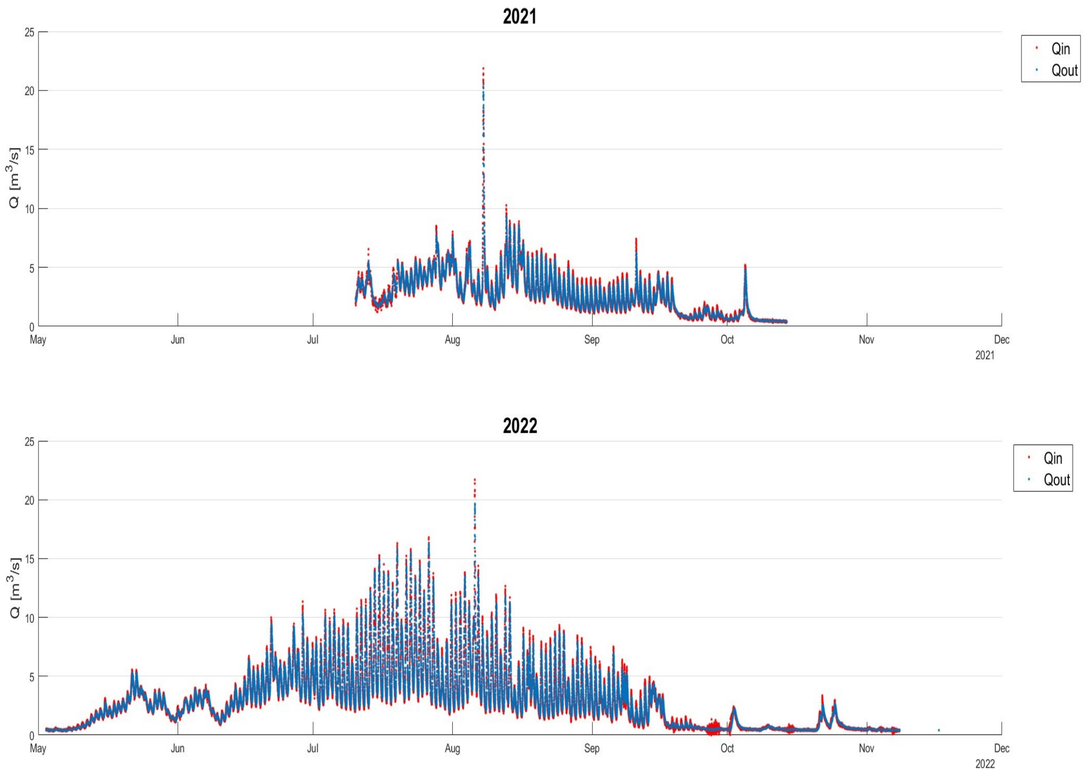

Figure 5.7: Inflow and outflow terms of the mass balance for Seracchi Lake. The dataset has a resolution of one value every 10 minutes, corresponding to the sampling period of the input data.

on August 5th at 22:40 when the Q_{IN} reached 21.7 $\mathrm{m^3\,s^{-1}}$. Interestingly, this exceptional event occurred around the same period as in 2021, but it did not stand out as prominently compared to the other values.

These observations align with the exceptional meteorological and climatic conditions of that year. The winter period was notably dry, resulting in limited precipitation, while the ablation period was prolonged and intense. The higher values of Q_{IN} during the summer of 2022 can be interpreted as a proxy for increased glacier melting due to these unique weather and climate conditions.

5.4 Lake dynamics

Once the hydrology of the lake was established, further investigation was conducted to deepen the understanding of its dynamics.

A lake acts as a natural buffer, absorbing and regulating the inflows from precipitation and glacial meltwater. This process, known as lamination, helps mitigate the impacts of rapid inflow fluctuations on downstream areas. The lamination capacity is determined by the lake's physical characteristics, such as size, depth, and surface area. A large surface area facilitates increased evaporation, while the depth determines the volume of water that can be stored. Consequently, a lake has the potential to reduce peak flows downstream and prevent potential flooding events during periods of high inflows. Conversely, during periods of low inflows, a lake can release stored water, ensuring a more consistent downstream flow and maintaining ecological balance.

External factors, such as precipitation and temperature, strongly influence the lake's inflows and outflows. Precipitation significantly impacts inflows, while temperature affects both the inflows through increased melting and the outflows through increased evaporation rates.

By analyzing the lake's response to different inflow patterns and its ability to modulate outflows, valuable information can be obtained.

The lamination capacity of Seracchi Lake was investigated by distinguishing between two main conditions: "dry days" and "wet days." Dry days refer to periods without recorded precipitation events, where the lake's inflows are primarily sourced from tributaries and glacier meltwater. The inflow patterns during dry days are expected to follow a seasonal cycle, reflecting the variations in glacier melting. On the other hand, wet days are characterized by the absence of rainfall events. During these days, the lake's response to a rainfall event is influenced by factors such as the initial water level, as well as the intensity and duration of the precipitation.

A lake's capacity to modulate the flow of water can be detected by analyzing the differences between the Q_{IN} and Q_{OUT} hydrographs. For example, if the inflow discharge (Q_{IN}) exceeds the outflow discharge (Q_{OUT}) during a particular period, it indicates that the lake is storing water and reducing the peak flow downstream. On the other hand, if the outflow discharge exceeds the inflow discharge, it suggests that the lake is releasing stored water to ensure a more consistent downstream flow.

In the case of Seracchi Lake, three indicators were derived:

1. Difference (D): This indicator represents the difference in value between the daily maximum input discharge and the daily maximum output discharge.
2. Time delay (T_d): This indicator measures the time needed for the output discharge to reach its peak after the maximum input discharge has already occurred.
3. Retention volume (W): This indicator quantifies the amount of water that the lake can retain before entering the source phase. It is calculated as the area between the Qin and Qout curves from the start to the end of the sink phase.

By using these indicators, it becomes possible to compare and evaluate the performance of Seracchi Lake under different hydrological conditions. Additionally, these indicators can be used to monitor any variations or trends over time, providing valuable information about the lake's lamination capacity and its role in regulating water flow.

5.4.1 Dry days

The input data for this analysis consists of the Q_{IN} and Q_{OUT} terms obtained from the mass balance calculations.
During dry days, when no runoff is present, the Q_{IN} term represents the combined inflow from the two tributaries. Since this water primarily originates from glacial melting, it is expected to exhibit a seasonal cycle that aligns with the patterns of glacial meltwater. In early summer, when the snowpack is still intact and the melt is minimal, the Q_{IN} values are expected to be low. As the summer progresses and the snow begins to melt, the glacial meltwater increases, leading to higher Q_{IN} values, peaking in the middle of summer. Towards September, as the melting period nears its end, the Q_{IN} values start to decrease, eventually reaching the minimum for the season.

Based on this hypothesis, the objective was to understand the average behavior of the lake during the summer period on days without any precipitation events. The dataset was divided into two summers: 2021, spanning from July 10, 2021, to September 22, 2021 (incomplete due to the lack of input data), and 2022, spanning from June 21, 2022, to September 22, 2022. There were fewer dry days in 2021 compared to 2022, with a total of 36 days compared to 64 days in 2022.
The mass balance data corresponding to these dry days were then extracted, and each of its term was averaged to obtain an "average dry day" representing the typical hydrological dynamics within a 24-hour period for the given summer season. The resulting hydrographs for 2021 and 2022 are depicted in Figure 5.8 and Figure 5.9.

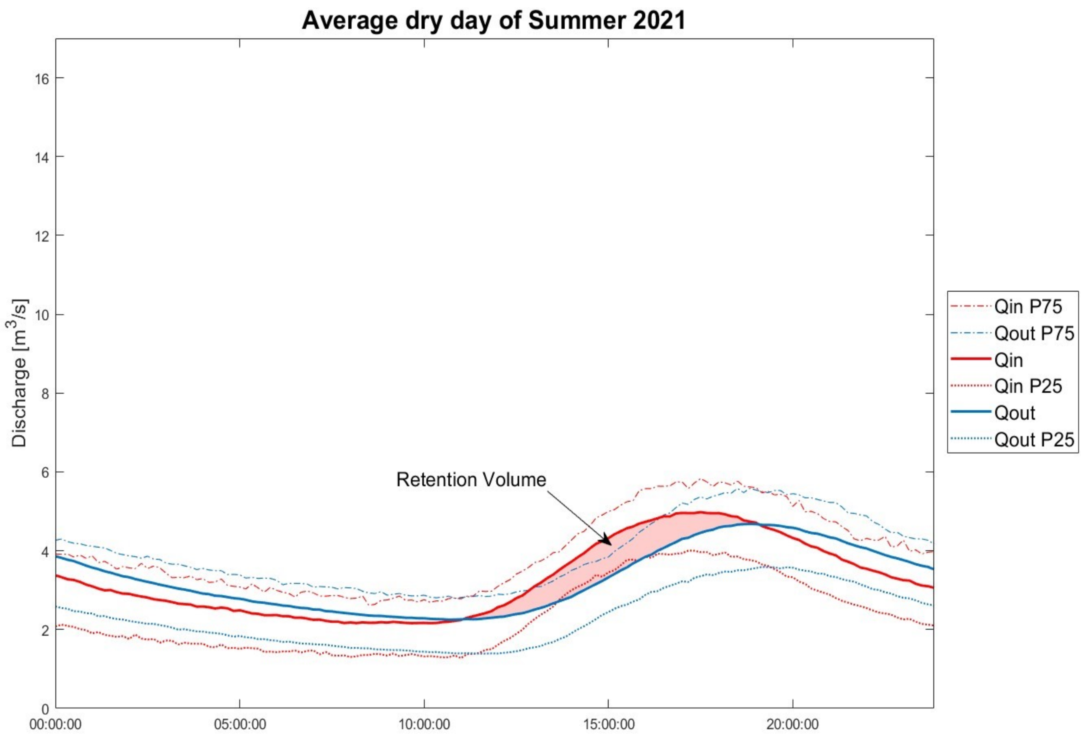

Figure 5.8: Q_{IN} and Q_{OUT} hydrographs illustrating the average behavior of Seracchi Lake during a dry day in the summer period of 2021. The dashed lines represent the variability of the values from the mean, expressed in terms of the 75th percentile and 25th percentile.

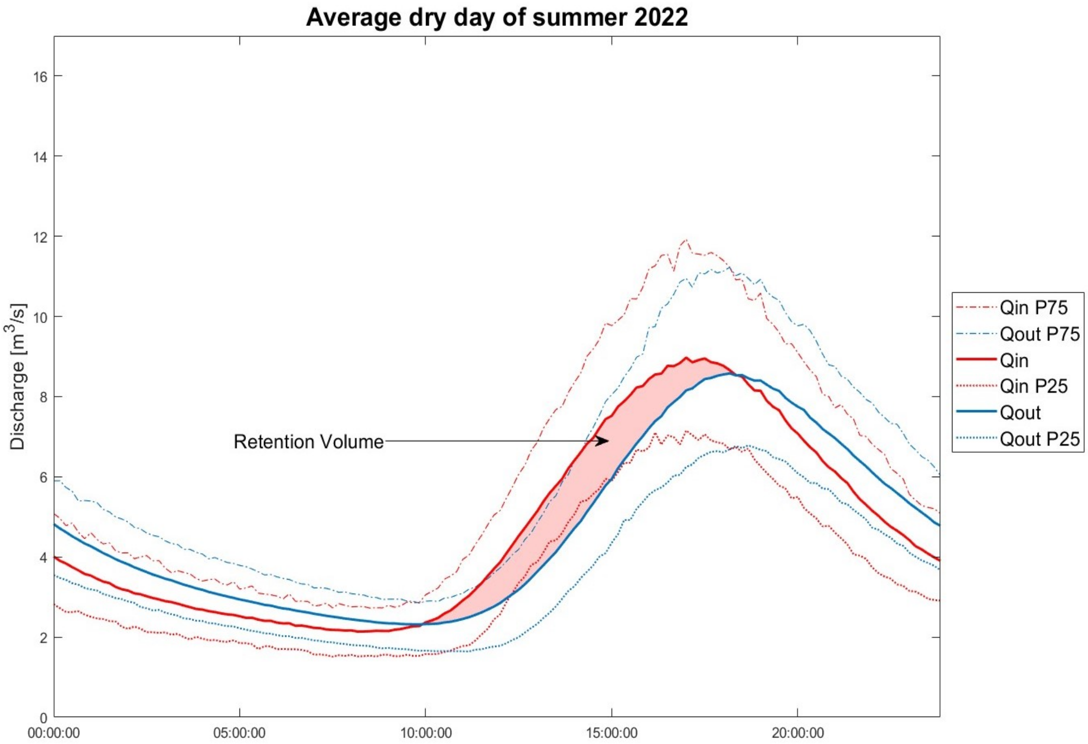

Figure 5.9: Q_{IN} and Q_{OUT} hydrographs illustrating the average behavior of Seracchi Lake during a dry day in the summer period of 2022. The dashed lines represent the variability of the values from the mean, expressed in terms of the 75th percentile and 25th percentile.

The D, T_d, and W parameters were calculated for these two average days, and their values are reported in Table 5.1. By analyzing the variations in these parameters across the two years, valuable insights into the interannual dynamics can be gained.

On the hydrographs, it can be observed that the maximum inflow (Qin) occurs around the same time window, between 17:00:00 and 17:30:00, for both 2021 and 2022. Additionally, the time delay between the maximum inflow (Q_{IN}) and the maximum outflow (Q_{OUT}) remains relatively constant, with a difference of around 10 minutes between the two years, which is considered negligible.

When comparing the other two parameters, a difference of 0.1 $m^3\,s^{-1}$ is observed in the D values between 2021 and 2022, while the retained volume (W) shows a significant change, nearly doubling in 2022 compared to 2021, despite the similar duration of the sink phase, which is approximately 8 hours.

	Parameters				
	D [$m^3 s^{-1}$]	$timemax_{IN}$ [h]	$timemax_{OUT}$ [h]	T_d [h]	W [m^3]
2021	0.2983	17:30:00	18:50:00	1:20:00	1.6807e+04
2022	0.3933	17:00:00	18:10:00	01:10:00	3.0634e+04

Table 5.1: of Seracchi Lake dynamics describing parameters for the years 2021 and 2022. The table presents the values of the D, T_d, and W parameters for the average 2021 and 2022 dry days. The D parameter represents the average difference between the maximum inflow and outflow rate expressed in $m^3 s^{-1}$. The T_d indicates the time delay between peak inflow and peak outflow in hours. The W parameter represents the retained volume of water in m^3.

From these results, it can be inferred that on average, the lake is capable of delaying the peak in outflow by approximately 1 hour. Furthermore, the disparity in values for D and W implies that these parameters are influenced by the magnitude of Q_{IN}. Higher inflows result in a greater influx of water into the lake, which is temporarily stored. The duration of the sink phase averages around 8 hours, after which the retained volume begins to be released downstream. The source phase, characterized by outflow exceeding inflow, lasts twice as long as the sink phase. Notably, in both 2021 and 2022, the Q_{OUT} value just prior to the initiation of the sink phase was 2.3 $m^3 s^{-1}$.

To investigate the seasonal pattern, the dataset for each year was further divided into subsets corresponding to two-week periods. The specific dates and dry days for each subset are provided in Table 5.4. The average daily behavior was calculated for each subset, and the respective hydrographs can be found in Appendix A.

	Dry days	
	2021	2022
15-30 June	/	/
1-15 July	/	13
16-31 July	6	12
1-15 August	8	11
16-31 August	12	11
1-15 September	8	7

Table 5.2: In the table, the two-week periods into which the dataset has been divided and the respective dry days are indicated. For June 2021, there is no data available. The recording starts on July 10, 2021, but there are no dry days until the 15th. Therefore, the July 1-15 subset has also been excluded. Similarly, for the June 15-30, 2022, there were only 3 dry days, which is not a significant number for analysis. Hence, this subset has also been omitted. In total, 9 subsets have been considered for analysis.

The parameters D, T_d, and W were calculated for each average day and are presented in Table 5.3. Upon examining the data from 2021, it becomes apparent that the first subset deviates noticeably from the others. This discrepancy can be attributed to the fact that the dataset for this particular subset comprises only 6 days, which may not have provided enough data points for the averaging process to effectively smooth out the results. However, the data from all the other subsets exhibit consistent patterns and behavior. Consequently, these remaining subsets will serve as the reference for further analysis. When analyzing the variations in the values, it is possible to observe both the inter-seasonal dynamics by comparing different periods within the same year and the inter-annual dynamics by comparing the same period across different years.

In both 2021 and 2022, the peak inflow (Q_{IN}) occurs between 5 p.m. and 5:30 p.m. Throughout the 2021 season, the variability in the time delay is minimal and can be neglected. On average, the T_d in 2021 is approximately 1.5 hours, consistent with the overall average data. In contrast, the summer season of 2022 exhibits greater variability in the time delay. Specifically, during the periods from July 1st to July 15th and from August 1st to August 15th, the time delay is less than 1 hour, indicating a shorter duration between peak inflow and peak outflow.

	Parameters				
	D [$m^3\,s^{-1}$]	timemax$_{IN}[h]$	timemax$_{OUT}[h]$	T_d [h]	W [m^3]
2021	0.1811	18:50:00	21:10:00	02:20:00	1.2750e+04
	0.2814	17:00:00	18:40:00	01:40:00	1.6075e+04
	0.4043	17:30:00	18:50:00	01:20:00	2.0044e+04
	0.4153	17:10:00	19:00:00	01:50:00	1.8829e+04
2022	0.3375	17:40:00	18:20:00	00:40:00	3.3274e+04
	0.3666	17:00:00	18:10:00	01:10:00	3.8994e+04
	0.4657	17:00:00	17:30:00	00:30:00	3.6666e+04
	0.5542	17:00:00	18:30:00	01:30:00	3.3938e+04
	0.4965	17:20:00	18:40:00	01:20:00	2.5196e+04

Table 5.3: Summary of Seracchi Lake dynamics describing parameters for each two-week subset. This table presents the values of parameters D, T_d, and W calculated for each two-week subset within the summer seasons of 2021 and 2022. The subsets are organized chronologically, corresponding to specific periods of the summer season.

Examining the difference between the peak inflow (Q_{IN}) and peak outflow (Q_{IN}) shown in the Figure 5.10, it is evident that both 2021 and 2022 exhibit a similar seasonal cycle. The difference between these two values increases as the season progresses, reaching its peak in the last fifteen days of August. However, the values in 2022 have doubled compared to 2021, indicating higher inflow rates.

Another notable difference between the two years is observed in the W values, representing the retained volume. In 2022, the W value was 85% higher than the value recorded in 2021.
Additionally, the seasonal behavior depicted in Figure 5.11 shows distinct patterns between the two years. In 2021, the values increase as the season progresses, reaching their peak in August, and then remain relatively constant until September. In contrast, in 2022, the peak is reached earlier, at the end of July. This discrepancy in the timing of the peak is consistent with the dynamics of the inflows and is aligned with the Rutor glacier mass balance (refer to Figure **??**). Historical data

suggests that by July 2022, the ablation registered for the entire hydrological year of 2020-2021 had already been surpassed, which contributes to the earlier peak in inflows observed in the end of July.

In conclusion, this analysis provides a comprehensive understanding of the lake's behavior during the summer season and offers valuable insights about the lake's response to glacial melting and its ability to regulate the inflow and outflow processes.

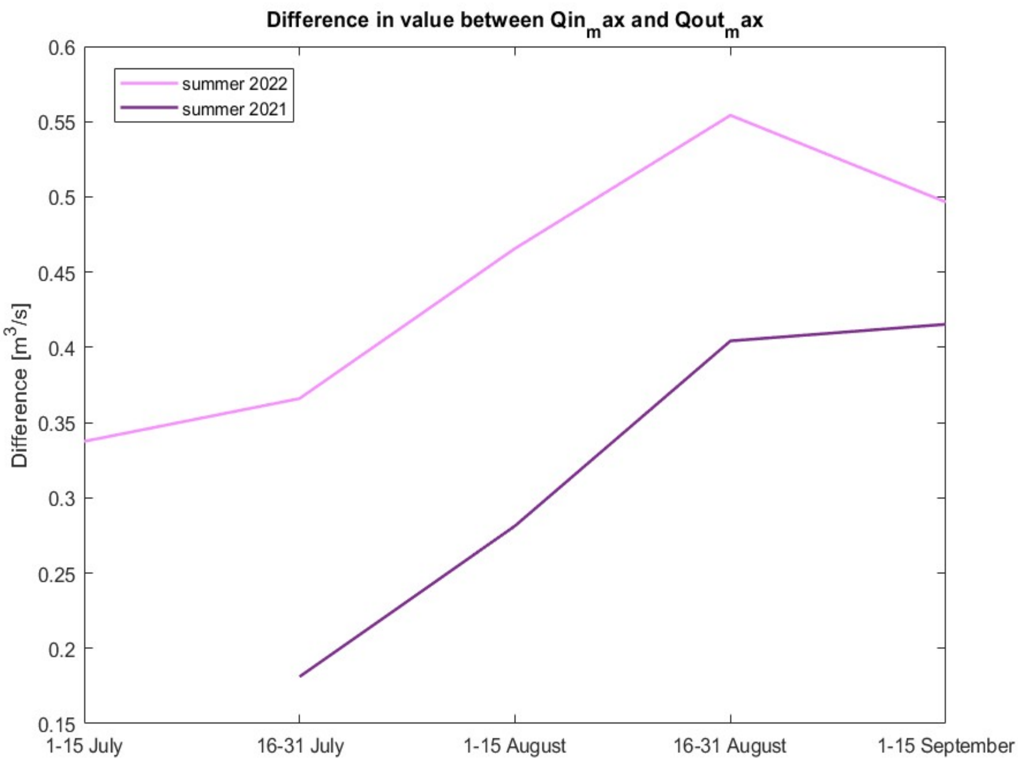

Figure 5.10: Comparison of the difference between peak inflow (Q_{IN}) and peak outflow (Q_{OUT}) values obtained for each the two-weeks period of summer 2021 and 2022. Both years exhibit a similar seasonal cycle.

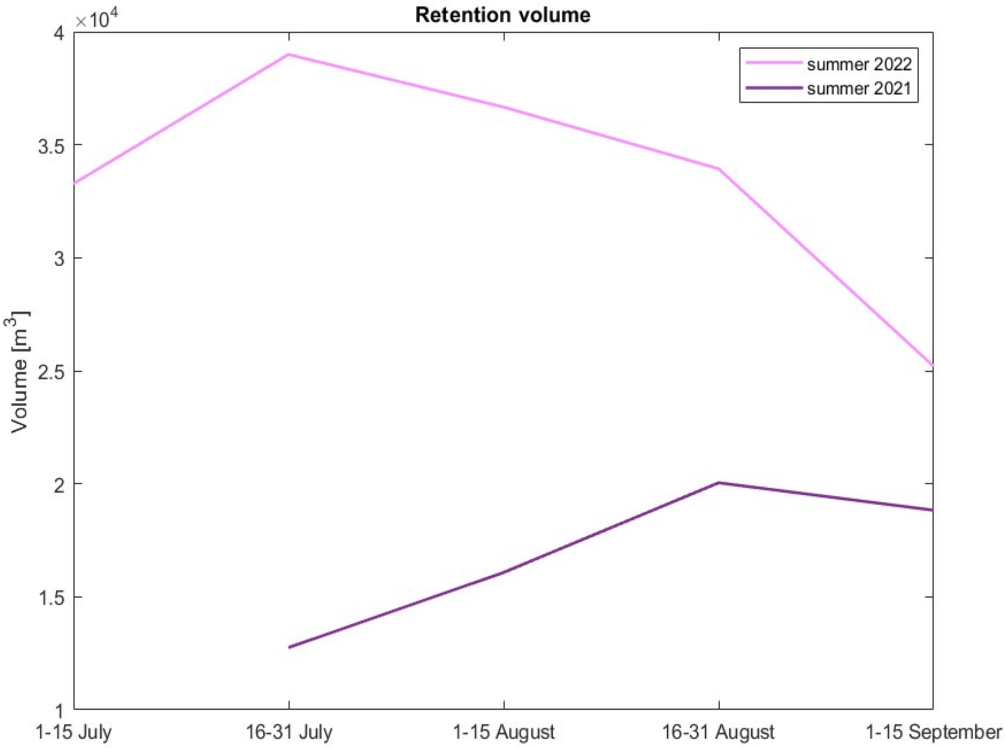

Figure 5.11: Comparison of the retention volume (W) values obtained for each the two-weeks period of summer 2021 and 2022.

Temperature - Inflow correlation

The results obtained so far highlight a significant increase in inflow discharge values in 2022 compared to 2021 and a dependence of the lake dynamics on the increased glacial ablation rate. To further investigate this hypothesis, the correlation between temperature and inflow discharge during dry days was examined, as dry days provide a clearer representation of the meltwater-driven inflows.

Two approaches were employed to explore this correlation.
The first approach involved analyzing the relationship between higher temperatures and the peak inflow (Q_{IN}) observed during each dry day. It was observed that the maximum Q_{IN} value typically occurs around 5 p.m. Given the location of the Rutor Glacier, it can be inferred that the glacier is exposed to sunlight from approximately 8 a.m. to 2 p.m. Therefore, the peak inflow occurs when the

glacier has experienced the hottest period of the day. For each dry day during the summer seasons of 2021 and 2022, the temperature values recorded between 8 a.m. and 2 p.m. were collected and averaged. The correlation between these average temperature values and the correspondent daily maximum Q_{IN} values was then examined. The results depicted in Figure 5.12 demonstrate a clear correlation, with a correlation coefficient of 0.5791 for 2021 and 0.8406 for 2022, indicating a stronger correlation in 2022.

The second approach involved comparing the daily mean temperature with the daily mean Q_{IN} value. For each dry day, the average temperature and Q_{IN} values recorded between 00:00:00 and 23:59:00 were calculated and analyzed. The correlation between these values was investigated, revealing a strong correlation. In 2021, the correlation coefficient was found to be 0.6272, while in 2022, it increased to 0.8218. The corresponding correlation graph is presented in Figure 5.13.

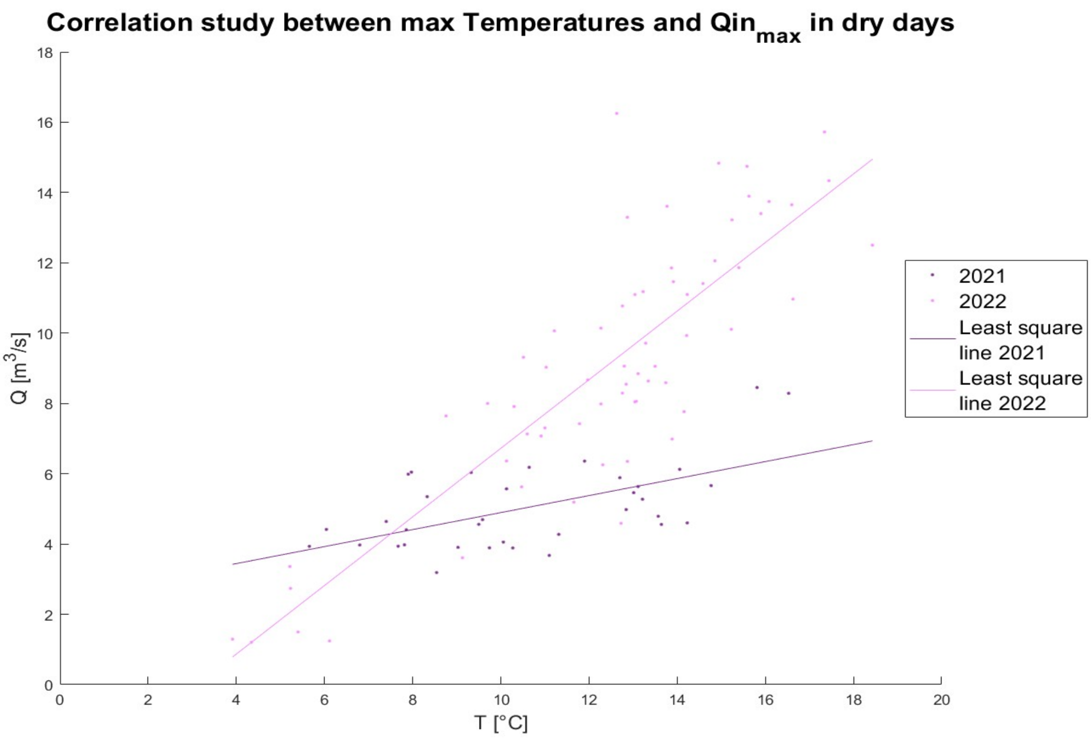

Figure 5.12: Correlation between the average of the daily higher temperature values recorded between 8 a.m. and 2 p.m. and daily maximum inflow (Q_{IN}) values during dry days in 2021 and 2022. The correlation index is 0.5791 for 2021 and 0.8406 for 2022, indicating a stronger correlation in 2022.

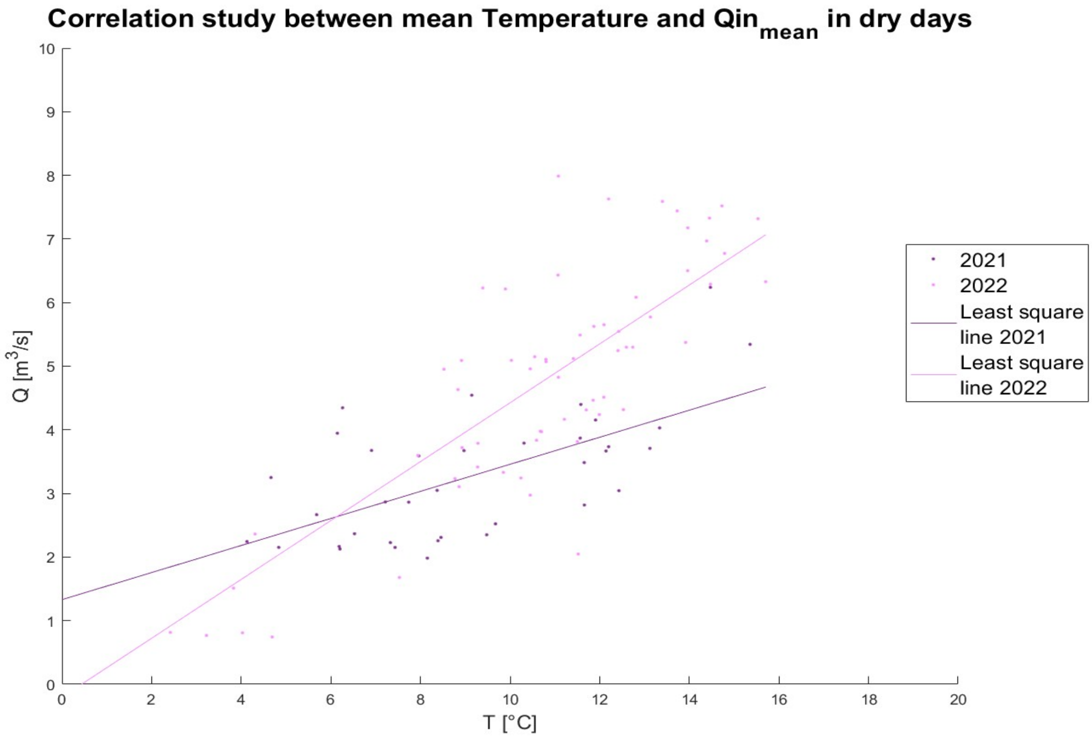

Figure 5.13: Correlation between mean temperature values and mean inflow (Q_{IN}) values during dry days in 2021 and 2022. The correlation index is 0.6272 for 2021 and 0.8218 for 2022, indicating a stronger correlation in 2022.

These results provide additional evidence to support the hypothesis of using the lake as a proxy for detecting glacier dynamics.

5.4.2 Wet days

The condition of a dry day is determined by the absence of rainfall events. Hourly precipitation data collected at La Thuile - La Grande Tête meteorological station, owned by ARPA VDA (Regional Environmental Protection Agency of Valle d'Aosta), were used for this analysis (refer to Section 3.4).

As for dry days, the dataset was divided into two summer periods: 2021, spanning from July 10, 2021, to September 22, 2021, and 2022, spanning from June 21, 2022, to September 22, 2022. The days with recorded precipitation values greater than 0 mm were selected. The dataset comprised 45 days in summer 2021 and 29 days in summer 2022.

Given the variability in the lake's response to precipitation events, it was not possible to derive an average seasonal dynamic for these days. The lake's response depends on various factors, including its initial condition and the intensity and duration of the precipitation event.
To capture the representative behavior of the lake, a selection of notable events from the dataset was made. Figure 5.14 depicts the precipitation dataset along with the corresponding Q_{IN} and Q_{OUT} hydrographs for the summer of 2021. Similarly, Figure 5.15 shows the corresponding graphs for the summer of 2022.

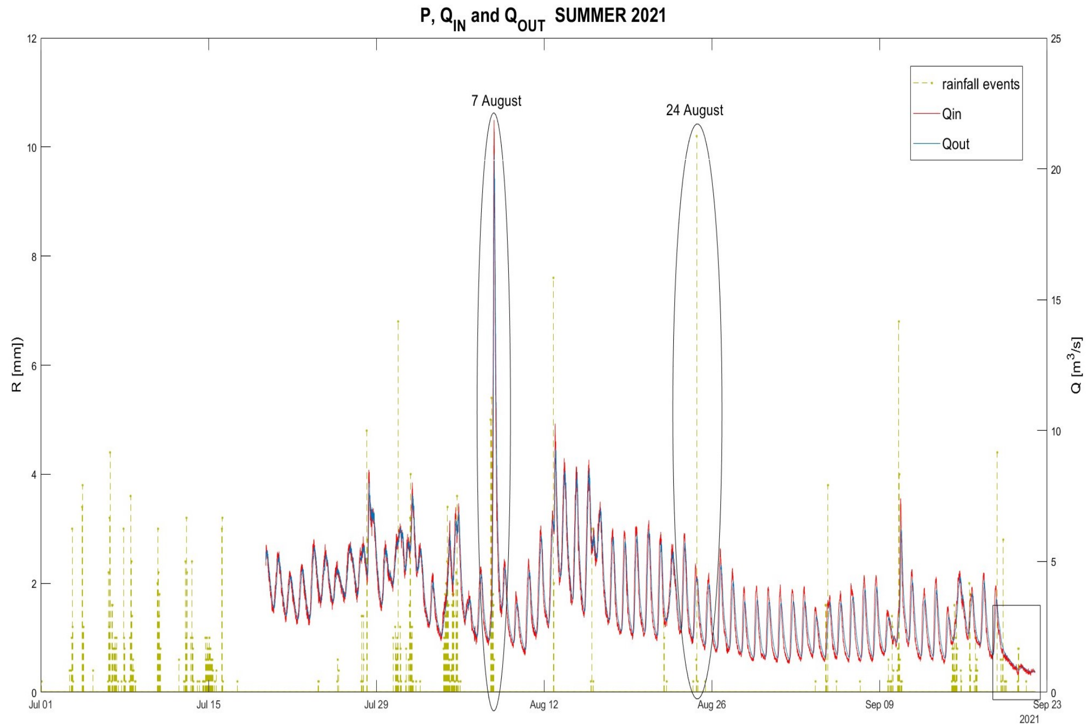

Figure 5.14: Comparison of precipitation data with Q_{IN} and Q_{OUT} hydrographs for the summer of 2021. Highlighted precipitation events showcase different lake response patterns, including the event with the highest intensity in the season and an event with high intensity that did not result in a significant increase in the hydrographs.

The highlighted precipitation events in the Figures 5.14 and 5.15 were chosen to include both the event with the highest intensity in the season and the event associated with the highest inflow in the season. Additionally, an event with high-intensity precipitation but no corresponding increase in the Q values was selected. They are summarized in the following Table 5.4.

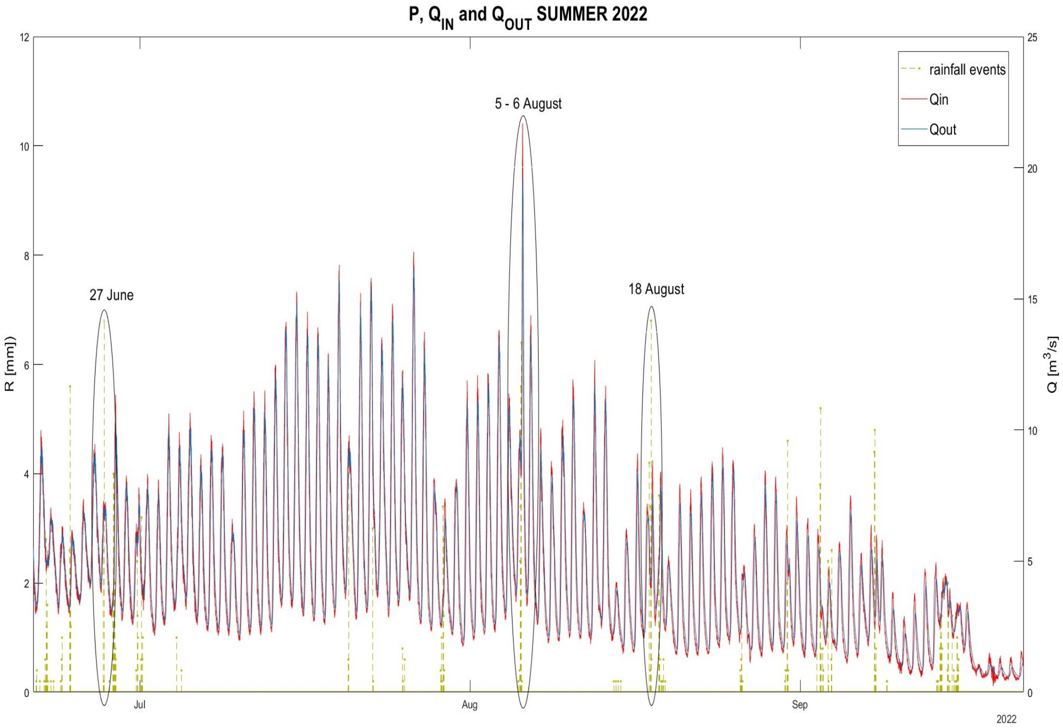

Figure 5.15: Comparison of precipitation data with Q_{IN} and Q_{OUT} hydrographs for the summer of 2022. Highlighted precipitation events showcase different lake response patterns, including the event with the highest intensity in the season and an event with high intensity that did not result in a significant increase in the hydrographs.

	2021	2022
Max P Intensity	24 Aug	27 Jun
Max Q	7 Aug	5/6 Aug
High P Low Q	10 Sept	18 Aug

Table 5.4: Summary of selected precipitation events.

A zoom on the daily dynamics is presented in Figure 5.16 and 5.17. On those graphs the temperature and precipitation patterns were added. Moreover, the inflows and outflows of the nearest dry day are depicted with dashed line as reference.

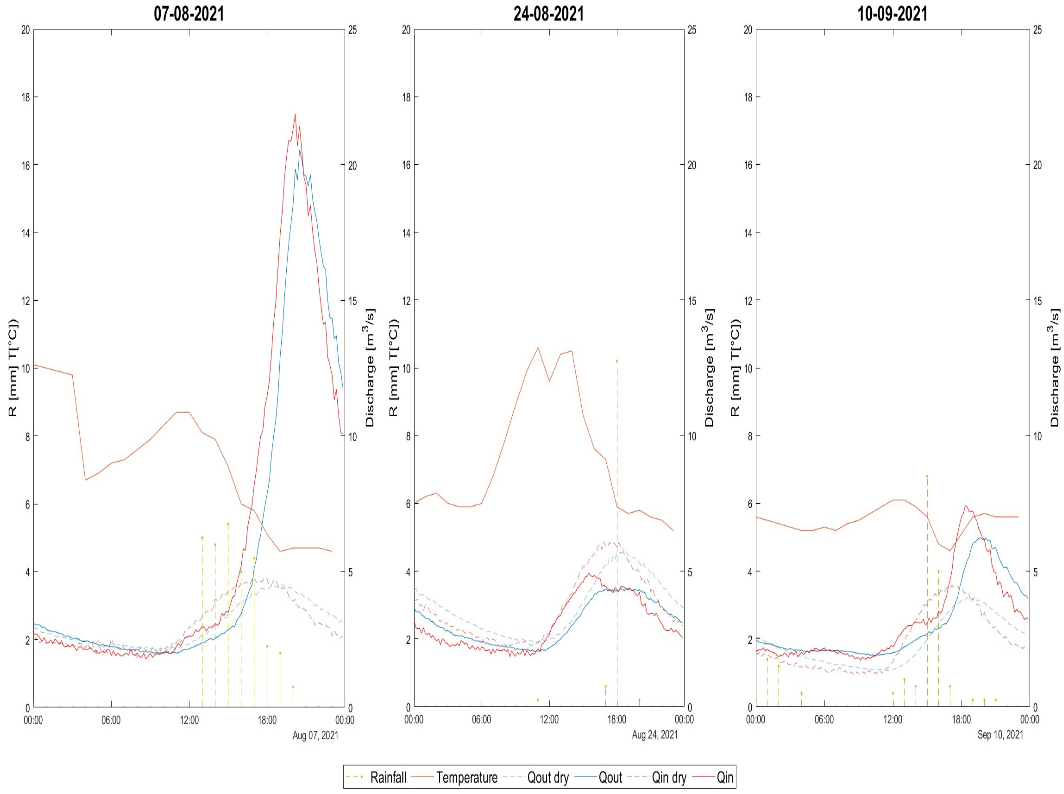

Figure 5.16: Zoomed-in view of the daily dynamics during the selected precipitation event in 2021. The graph includes temperature and precipitation patterns, along with the inflows and outflows of the nearest dry days depicted with dashed lines as a reference.

For each day considered, the three parameters characterizing the dynamics of Seracchi Lake were calculated and are reported in Table 5.5. The D parameter represents the difference between the maximum inflow and outflow rate expressed in $\mathrm{m^3\,s^{-1}}$. The T_d indicates the time delay between peak inflow and peak outflow in hours. The W parameter represents the retained volume of water in $\mathrm{m^3}$.

Based on these results, the following considerations can be made:

- On August 7, 2021, when the highest value of Q_{IN} is recorded, it rained for a long duration, approximately 7 hours. The rainfall started before the peak in Q_{IN} occurred, and for the first 4 hours, the intensity was greater than 4 $\mathrm{mm\,h^{-1}}$. These combined factors led to a peak in both Q_{IN} and Q_{OUT} values. The timing of these peaks is delayed compared to an average dry summer day

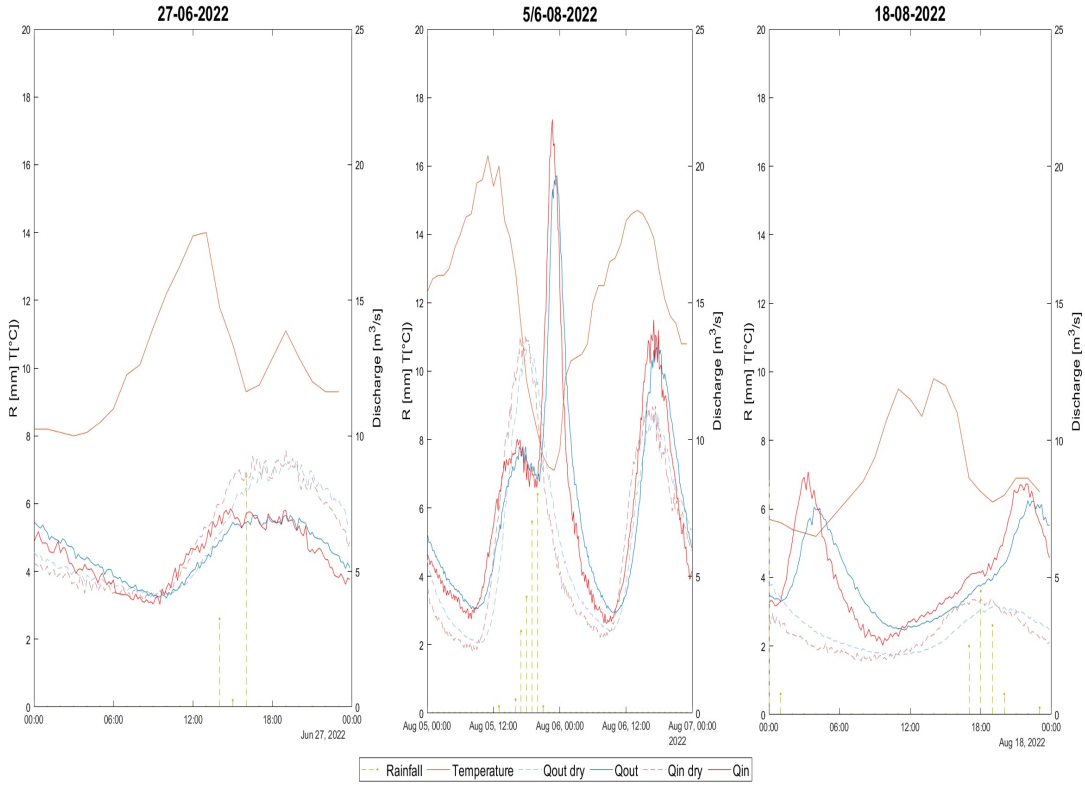

Figure 5.17: Zoomed-in view of the daily dynamics during the selected precipitation event in 2022. The graph includes temperature and precipitation patterns, along with the inflows and outflows of the nearest dry days depicted with dashed lines as a reference.

in 2021, with the peak Q_{IN} occurring at 20:10:00 and a time delay of only 20 minutes. The other two parameters, D and W, are significantly higher than the values of an average dry summer day in 2021, especially the retention volume (W). The exceptionality of this event can be observed by comparing the values of the hydrographs with those of the nearest dry day.

- On August 24, 2021, the most intense rainfall event of the 2021 season occurred, along with other smaller rainfall events. This event was recorded at 18:00:00 when the maximum Q_{IN} had already occurred. The day was characterized by higher temperatures compared to the other 2021 days considered, and the inflow and outflow values were generally lower than those of the nearest dry day. These factors combined resulted in the exceptional precipitation event

	Parameters				
	D [$m^3\,s^{-1}$]	timemax$_{IN}[h]$	timemax$_{OUT}[h]$	T_d [h]	W [m^3]
2021	1.3127	20:10:00	20:30:00	00:20:00	6.4828e+04
	0.5569	15:30:00	19:00:00	03:30:00	1.6424e+04
	1.1786	18:20:00	19:40:00	01:20:00	2.5872e+04
2022	0.2445	14:50:00	16:50:00	02:00:00	1.3849e+04
	2.0656	22:40:00	23:30:00	00:50:00	3.5974e+04
	1.3544	03:20:00	04:10:00	00:50:00	2.2959e+04

Table 5.5: Summary of Seracchi Lake dynamics describing parameters for each two-week subset. This table presents the values of parameters D, T_d, and W calculated for each two-week subset within the summer seasons of 2021 and 2022. The subsets are organized chronologically, corresponding to specific periods of the summer season.

not sustaining the peak Q_{IN}. Following the typical behavior, Q_{IN} increased to its maximum and then started to decrease. When the rain event occurred, Q_{IN} began to increase again, but to a new maximum, which was lower than the initial peak. Similarly, Q_{OUT} reached its maximum at the same time as the extreme event, leading to a sourcing phase with a higher Q_{OUT}. As a result, the time delay is 3 hours, which is higher than that recorded during an average dry day. The magnitude difference is the smallest among the 2021 wet days considered, as well as the retention volume. Moreover, the values of these parameters resemble those of the dry days.

- On September 10, 2021, a high number of rainy events occurred, but only two of them had significant intensity, exceeding 4 $mm\,h^{-1}$. These events were scattered throughout the day, with the most significant ones occurring before the peak in Q_{IN}. The temperatures on this day were the lowest among the 2021 wet days considered. The hydrographs do not show a significant peak, but the values of Q_{IN} and Q_{OUT} are nearly double those of the nearest dry day. Additionally, the D and W parameters are greater than those of the average 2021 dry day, while the time delay is in line with the dry days.

- On June 6, 2022, the rain event with the highest intensity of the summer 2022 occurred. It was recorded at 4 p.m. after only two small rainy events. The event happened after the peak Q_{IN} occurrence, which is unusually early compared to the average dry day in 2022. The temperatures on this day were the second highest among the the 2022 wet days under consideration, and the hydrographs showed lower values than the nearest dry day. The time delay between the peak Q_{IN} and Q_{OUT} was 2 hours, higher than the value observed on dry days. This is consistent with the fact that the outflows are sustained by precipitation and peak later. However, the W and D parameters did not differ significantly from the values observed on the dry days.

- On August 5, 2022, the highest peak in Q_{IN} occurred. The hydrograph includes two days because the event occurred around midnight, and its effects could only be observed afterward. Prior to the event, there were other rainfall events with increasing intensity. The rainfall started when Q_{IN} was approaching its peak, and the event with the highest intensity occurred after the peak. The temperatures on this day were very high, the highest among the sampled days. As a result, the August 5th Q_{IN} and Q_{OUT} hydrographs followed a similar pattern to the nearest dry day, but at lower values, until 8 p.m.. At this point, the discharges increased again to a new maximum, higher than the previous peaks and the highest of the season. The time delay between these peaks was lower than the average, the D parameter was much higher, while the W parameter was consistent with the dry days.
  Comparing these dynamics to those of August 7, 2021, it is clear that these peaks in inflows were the result of consecutive events with high intensity affecting the area. Furthermore, the fact that the retention volume was so high in 2021 can be explained by the event sustaining the sink phase flow, whereas in 2022, the event occurred during a period of low Q_{IN}.

- On August 18, 2022, an event with an intensity higher than 6 $\mathrm{mm\,h^{-1}}$ occurred at 00:00:00. It caused a nighttime peak in the Q_{IN} and Q_{OUT} hydrographs. The maximum Q_{IN} for the day was recorded at 03:20:00, after which the values started to decrease and then increase again during the day, although with a delay compared to the typical pattern. The Q_{OUT} followed a similar

path.
Between the peaks in Q_{IN} and Q_{OUT} caused by the precipitation, the time delay was 50 minutes, slightly less than observed on dry days. The difference in magnitude between the peaks was higher than on dry days, while the retention volume was not as high compared to that of dry days. However, it is important to consider that this additional volume is stored in the lake during a period when the Q_{IN} values are usually low.

In summary, the summer of 2022 had fewer rainy events, higher temperatures, and higher values of inflow and outflow compared to 2021. However, the factors influencing the response of the Seracchi Lake to precipitation events were consistent between the two years.
The timing and intensity of the events played crucial roles. If an event happened before the peak in Q_{IN}, it contributed to increasing its magnitude. Events that occurred immediately after the peak in Q_{IN} sustained the source phase, resulting in a broader shape of the hydrograph. While, events that occurred during the source phase, in periods of natural low flow, caused an immediate increase in the hydrograph, leading to a second peak in the discharges. Moreover, if the event is significant, but random, the response of the lake is not so evident, while prolonged exposure of the lake to intense precipitation cause greater picks.
Additionally, also temperatures seems to have an impact on the hydrographs, by influencing the lake initial state.

6 | Conclusion

The objective of this thesis was to enhance the understanding of the morphology, hydrology, and dynamics of Seracchi Lake in the Rutor proglacial area. Through the manipulation and integration of geomatic, geophysical, and hydrological data, along with meteorological data collected from 2021 to 2022, valuable insights into the lake's morphology and hydrology were obtained.

The reconstruction of the lake's bathymetry yielded significant results. The integration of geomatic data with Ground Penetrating Radar (GPR) data and the utilization of a two-step interpolation method allowed for addressing technical limitations in data collection in the first 20-30 cm depth. This approach maintained a high level of detail in the analysis and provided reliable results, particularly in the depth range that is most sensitive to water level oscillations.
The resulting bathymetry revealed a shallow lake with distinct morphological features in different parts. It extends between 2 376.0343 m a.s.l. and 2 387.004 m a.s.l.

The value of these results goes beyond their specific reliability, as they served as the foundation for studying the lake's hydrology. The relationship between the lake's morphology and water level was further investigated through the production of the Volume-Lake Water Level (V-H) and Area-Lake Water Level (A-H) curves. These curves provided insights into the variation of the lake's assets under different filling conditions, highlighting the progressive accumulation of water as the water level rises and the limitation in the expansion of the lake's surface area, likely related to the topography.
The definition of analytical functions that relate the lake's area and volume to the water level, with a high determination coefficient close to 1, is another significant achievement of this thesis. By knowing the water level, which can be easily measured, these functions enable the estimation of the lake's surface area and volume at a given time. This information has various practical applications. For

instance, by forecasting the lake's water level, it becomes possible to estimate the available water volume in the lake. Moreover, the inclusion of the 1.5 m zone above the free surface of the lake in the modeled area allows the curves to be used in modeling potential flood events. By considering this upper portion of the lake, the curves provide valuable insights into the behavior of the lake under extreme conditions, aiding in the assessment and prediction of flood dynamics.

To further investigate the hydrological dynamics of the lake, a mass balance analysis was conducted, resulting in the calculation of the inflow (Q_{IN}) timeseries and the analysis of the Q_{IN} and Q_{OUT} hydrographs. The data showed an increase in both inflow and outflow values in 2022, a year characterized by a scarcity of precipitation events. This suggests that the increase can be attributed to enhanced melting, which aligns with the observed regression at the front of the Rutor Glacier during the same year.

The hydrographs exhibited a consistent pattern, with the outflow (Q_{OUT}) being delayed and reduced in magnitude compared to the inflow (Q_{IN}). This behavior is a typical effect of the lamination action performed by the lake. To characterize these dynamics, three key parameters were investigated: D, T_d, and W. The D parameter represents the difference between the maximum inflow and outflow rates, measured in $m^3\,s^{-1}$. The T_d parameter indicates the time delay between the peak inflow and peak outflow, measured in hours. Lastly, the W parameter quantifies the volume of water retained in the lake, measured in m^3.
The analysis revealed that the lamination effect of Seracchi Lake leads to a delay of approximately one to one and a half hours in the peak outflows. This delay is influenced by the magnitude of the inflows, which affects also the values of D and W.

The study of these parameters, particularly by differentiating between dry and wet days, has provided valuable insights into the inter*annual and inter-seasonal dynamics of the Seracchi Lake.
Comparing the dry days of summer 2021 to the notably drier summer of 2022, significant differences have been observed. On average, the retention volume in 2022 was 82% higher than in 2021, indicating a greater temporary storage of water in the lake. Additionally, the difference between the maximum inflow and outflow

in 2022 was, on average, 32% higher compared to 2021. However, the time delay between the peak inflow and outflow remained relatively constant.
Furthermore, the D parameter exhibits a seasonal cycle, with the difference in values increasing as the season progresses and reaching its peak in the last 15 days of August. On the other hand, the retained volumes display distinct patterns between the two years. In 2021, the retained volumes peaked in the last 15 days of August, while in 2022, they reached their maximum between the 16th and 31st of July. These findings underscore the high sensitivity of Seracchi Lake to climate conditions, particularly the influence of glacial meltwater. Historical data reveals that by July 2022, the rate of ablation had already surpassed the cumulative ablation for the entire hydrological year of 2020-2021. The earlier peak in inflows and the corresponding increase in retained volumes can be attributed to this intensified melting process, highlighting the crucial role of glacial meltwater in driving the overall behavior of Seracchi Lake.

When examining wet days, the analysis has emphasized the importance of considering the timing and intensity of precipitation events in understanding the dynamics of Seracchi Lake. Events occurring before the peak in inflow (Q_{IN}) contribute to amplifying its magnitude, while events immediately following the peak sustain the source phase, resulting in a broader shape of the hydrograph. On the other hand, events during the source phase, when natural flow is low, lead to an immediate increase in the hydrograph, resulting in a second peak in discharges. It is important to note that if an event is significant but occurs randomly, the lake's response may not be as discernible. However, prolonged exposure to intense precipitation leads to more pronounced peaks in the lake's hydrograph.

In the end, the influence of temperature on the lake's dynamics was investigated. The correlation analysis conducted on dry days revealed strong relationships between temperature and inflow discharge. Both the maximum inflows and mean daily inflows exhibited significant correlations with temperature. These findings suggest the potential use of Seracchi Lake as a proxy for detecting glacier dynamics, as temperature is a key driver of glacial meltwater production.

In conclusion, this thesis has significantly contributed to the understanding of the hydrological dynamics of Seracchi Lake and its response to climate conditions.

The findings have provided valuable insights into the functioning of glacially-fed lakes and their interaction with the surrounding environment. However, it is important to acknowledge that this thesis represents an initial stage of research, and there are numerous opportunities for further investigation.
Future studies can build upon these findings and delve deeper into the Seracchi Lake system. One potential avenue is the development of a predictive model based on the reconstructed dynamics, incorporating variables from the mass balance. Such a model would enable the accurate prediction of the lake's behavior under different conditions.
Furthermore, the integration of additional data sources, such as sediment distribution, can enhance our understanding of the lake's dynamics and improve the accuracy of model predictions. Exploring the complex interactions between Seracchi Lake and its surrounding environment, including the influence of nearby glaciers, vegetation, and land cover, would provide a more comprehensive understanding of the system and its responses to environmental changes.

In summary, this thesis has successfully advanced our knowledge of Seracchi Lake and laid a solid foundation for further research and practical applications in the study of glacier-fed lake dynamics.

Bibliography

[1] Martin Beniston and Daniel et al. Farinotti. «The European mountain cryosphere: a review of its current state, trends, and future challenges». In: *The Cryosphere* 12.2 (2018), pp. 759–794 (cit. on pp. 1, 2).

[2] IPCC. *Special Report on the Ocean and Cryosphere in a Changing Climate*. Tech. rep. Intergovernmental Panel on Climate Change, 2019 (cit. on p. 1).

[3] Martin T. Dokulil. «Impacts of Climate Warming on Alpine Lakes». In: *Oxford Research Encyclopedia of Climate Science* (2022) (cit. on pp. 2, 4).

[4] Harry Zekollari, Matthias Huss, and Daniel Farinotti. «Modelling the future evolution of glaciers in the European Alps under the EURO-CORDEX RCM ensemble». In: *The Cryosphere* 13 (2019), pp. 1125–1146 (cit. on p. 2).

[5] Jonathan L Carrivick and Fiona S Tweed. «Proglacial lakes: character, behavior and geological importance». In: *Quaternary Science Reviews* 134 (2016), pp. 1–3 (cit. on pp. 3, 26).

[6] Dan H Shugar et al. «Rapid worldwide growth of glacial lakes since 1990». In: *Nature Climate Change* 8 (2018), pp. 879–884 (cit. on p. 4).

[7] CC-Glacier Lab. «Multidisciplinar approach for the study of endoglacial phenomena and mass balances». In: (). URL: `https://www.diati.polito.it/focus/dipartimento_di_eccellenza_sui_cambiamenti_climatici_2018_2022/laboratorio_multisito/cc_glacier_lab` (cit. on p. 4).

[8] Jonathan L Carrivick, Fiona S Tweed, Jenna L Sutherland, and Joseph Mallalieu. «Toward Numerical Modeling of Interactions Between Ice-Marginal Proglacial Lakes and Glaciers». In: *Frontiers in Earth Science* 4 (2016), p. 63 (cit. on p. 4).

[9] Sara Savi, Anuschka Buter, Tobias Heckmann, Joshua Theule, Luca Mao, and Francesco Comiti. «Multi-temporal analysis of morphological changes in an Alpine proglacial area and their effect on sediment transfer». In: *Catena* 220, Part B (Jan. 2023) (cit. on p. 5).

[10] Tom Müller, Stuart N. Lane, and Bettina Schaefli. «Towards a hydrogeomorphological understanding of proglacial catchments: an assessment of groundwater storage and release in an Alpine catchment». In: *Hydrology and Earth System Sciences* (2022) (cit. on p. 6).

[11] Franziska Maier and H. J. (Ilja) van Meerveld. «Long-term changes in runoff generation mechanisms for two proglacial areas in the Swiss Alps I: Overland flow». In: *Water Resources Research* 57 (2021), e2021WR030221. DOI: 10.1029/2021WR030221. URL: https://doi.org/10.1029/2021WR030221 (cit. on p. 6).

[12] Emmanuel Salim, Ludovic Ravanel, Philippe Bourdeau, and Philip Deline. «Glacier tourism and climate change: effects, adaptations, and perspectives in the Alps». In: *Regional Environmental Change* 21.120 (2021). DOI: 10.1007/s10113-021-01849-0 (cit. on p. 6).

[13] Cristina Viani and other. «Potential future lakes from continued glacier shrinkage in the Aosta Valley Region (Western Alps, Italy)». In: *Geomorphology* 69 (2020), pp. 1–15 (cit. on pp. 8–10).

[14] Cristina Viani, Nicola Colombo, Irene Maria Bollati, Giovanni Mortara, Luigi Perotti, and Marco Giardino. «Socio-environmental value of glacier lakes: assessment in the Aosta Valley (Western Italian Alps)». In: *Regional Environmental Change* 22 (2022) (cit. on pp. 8, 13, 14).

[15] A. Vergnano, C. Oggeri, and A. Godio. «Geophysical–geotechnical methodology for assessing the spatial distribution of glacio-lacustrine sediments: The case history of Lake Seracchi». In: *Earth Surface Processes and Landforms* (2023), pp. 1–24 (cit. on pp. 10, 11, 13, 14, 18, 19, 27).

[16] Giuseppe Orombelli. «Il Ghiacciaio del Rutor (Valle d'Aosta) nella Piccola Età Glaciale». In: *Geografia Fisica e Dinamica Quaternaria* Suppl. VII (2005), pp. 239–257 (cit. on p. 10).

[17] Fabio Villa, Valter Maggi, and Mattia De Amicis. «GIS analysis of Rutor Glacier (Aosta Valley, Italy) volume and terminus variations». In: *Supplementi di Geografia Fisica e Dinamica Quaternaria* 30 (Jan. 2007), pp. 87–95 (cit. on pp. 10, 13, 14).

[18] E. Corte et al. «Multitemporal characterisation of a proglacial system: a multidisciplinary approach». In: *Earth System Science Data Discussions* (2023). Preprint, in review. DOI: 10.5194/essd-2023-94. URL: https://doi.org/10.5194/essd-2023-94 (cit. on pp. 11, 13, 16, 20, 23).

[19] URL: https://www.arpa.vda.it/it/effetti-sul-territorio-dei-cambiamenti-climatici/ghiacciai/bilancio-di-massa (cit. on p. 11).

[20] URL: https://www.arpa.vda.it/it/archivio-news/3864-2022,-annus-horribilis-per-i-ghiacciai-alpini (cit. on p. 12).

[21] ARPA VDA. *Rilievi Glaciologici in Valle D'Aosta – anno 2022.* Tech. rep. Loc. Grande Charrière 44 - 11020 Saint-Christophe (AO), Valle d'Aosta, Italy: Agenzia Regionale per la Protezione dell'Ambiente (ARPA VDA), 2022 (cit. on p. 12).

[22] Chiara Colombero, Cesare Comina, Franco Gianotti, and Luigi Sambuelli. «Waterborne and on-land electrical surveys to suggest the geological evolution of a glacial lake in NW Italy». In: *Journal of Earth Science* 39.4 (Apr. 2014), pp. 547–555. DOI: 10.1007/s12583-014-0454-1 (cit. on p. 16).

[23] Luigi Sambuelli and Silvia Bava. «A GPR survey on a morainic lake in northern Italy for bathymetry, water volume and sediment characterization». In: *Journal of Applied Geophysics* 78.1 (June 2012), pp. 36–46. DOI: 10.1016/j.jappgeo.2011.09.016 (cit. on pp. 17, 18).

[24] Myrta Maria Macelloni, Elisabetta Corte, Andrea Ajmar, Alberto Cina, Fabio Giulio Tonolo, Paolo Felice Maschio, and Isabella Nicole Pisoni. «Multi-platform, Multi-scale and Multi-temporal 4D Glacier Monitoring. The Rutor Glacier Case Study». In: *DIATI - Department of Environmental, Land and Infrastructure Engineering, Politecnico di Torino* (2023) (cit. on p. 20).

[25] I. Henrico. «Optimal interpolation method to predict the bathymetry of Saldanha Bay». In: *Transactions in GIS* 25 (2021), pp. 1991–2009. DOI: 10.1111/tgis.12783 (cit. on p. 30).

[26] URL: https://gwlucastrig.github.io/TinfourDocs/NaturalNeighborIntro/index.html (cit. on pp. 30, 31).

[27] Tom Bobach. «Natural Neighbor Interpolation: Critical Assessment and New Contributions». Dissertation. Kaiserslautern: Technische Universität Kaiserslautern, Apr. 2008 (cit. on pp. 30, 31).

[28] Donald O. Rosenberry and Masaki Hayashi. *Surface Water - Groundwater Interaction: From Watershed Processes to Hyporheic Exchange.* Slides from the course held on May 15-19, 2023. Instructors: Dr. Donald O. Rosenberry, Colorado School of Mines, Golden, Colorado, U.S.A. and Dr. Masaki Hayashi, Department of Geoscience, University of Calgary, Alberta, Canada. 2023 (cit. on p. 38).

A | Seasonal subsets of daily average hydrographs

To analyze the seasonal variations, subsets of data were created by selecting two-week time windows for each year. They provide a more detailed understanding of the lake's hydrological dynamics throughout the year. The resulting plots are depicted in the following Figures.

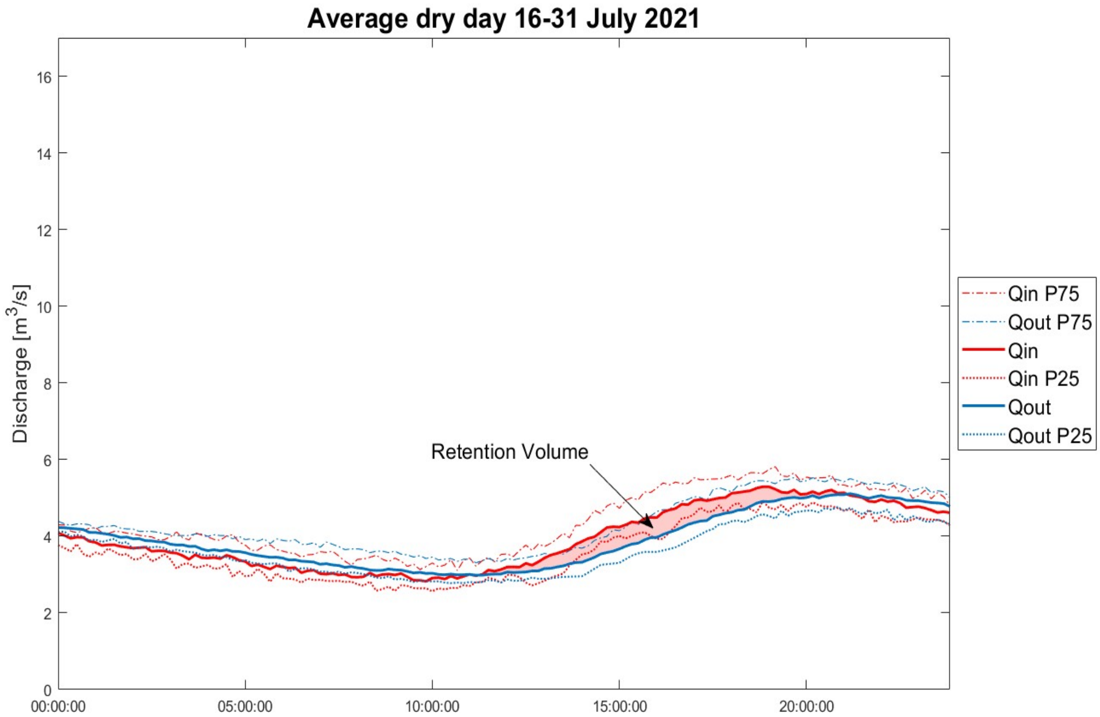

Figure A.1: Average dry day 16-31 July, 2021. Q_{IN} and Q_{OUT} hydrographs illustrating the average behavior of the Seracchi Lake inflows and outflows during a dry day occurred between 16-31 July 2021. The dashed lines represent the variability of the values from the mean, expressed in terms of the 75th percentile and 25th percentile.

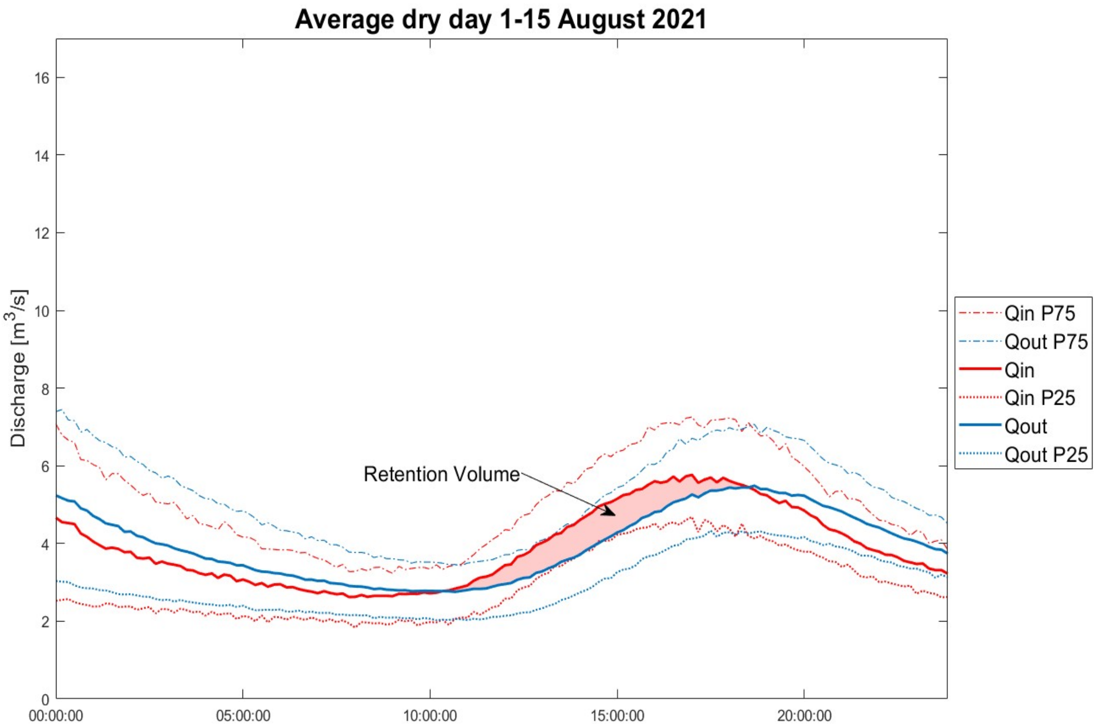

Figure A.2: Average dry day 1-15 August, 2021. Q_{IN} and Q_{OUT} hydrographs illustrating the average behavior of the Seracchi Lake inflows and outflows during a dry day occurred between 1-15 August 2021. The dashed lines represent the variability of the values from the mean, expressed in terms of the 75th percentile and 25th percentile.

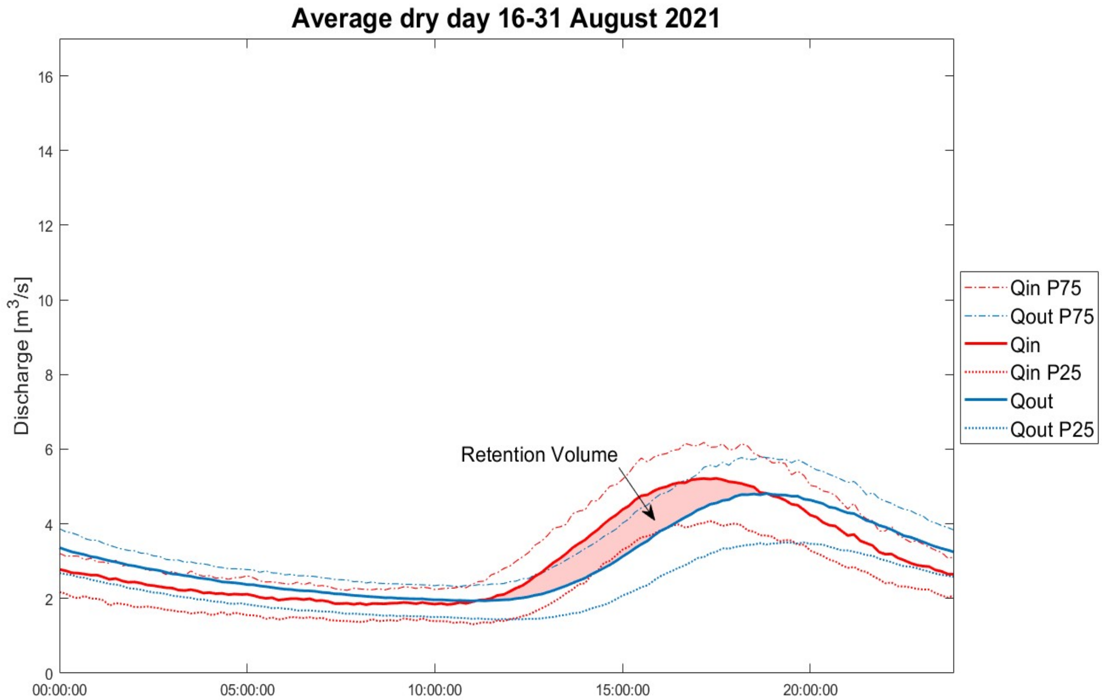

Figure A.3: Average dry day 16-31 August, 2021. Q_{IN} and Q_{OUT} hydrographs illustrating the average behavior of the Seracchi Lake inflows and outflows during a dry day occurred between 16-31 August 2021. The dashed lines represent the variability of the values from the mean, expressed in terms of the 75th percentile and 25th percentile.

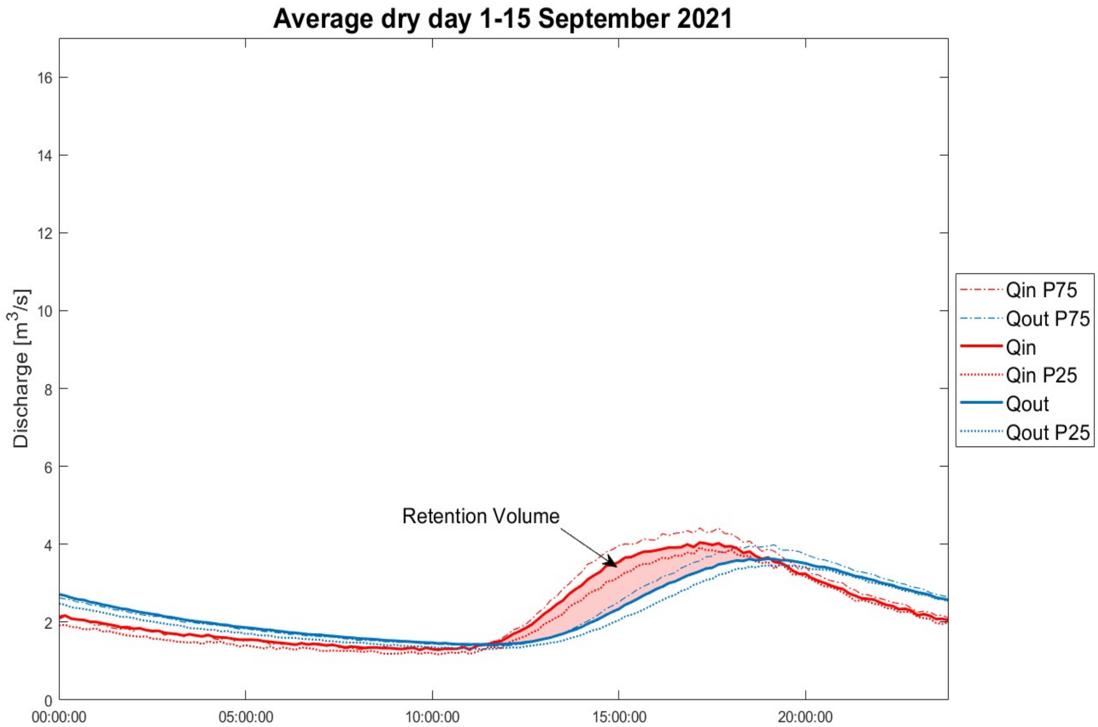

Figure A.4: Average dry day 1-15 September, 2021. Q_{IN} and Q_{OUT} hydrographs illustrating the average behavior of the Seracchi Lake inflows and outflows during a dry day occurred between 1-15 September 2021. The dashed lines represent the variability of the values from the mean, expressed in terms of the 75th percentile and 25th percentile.

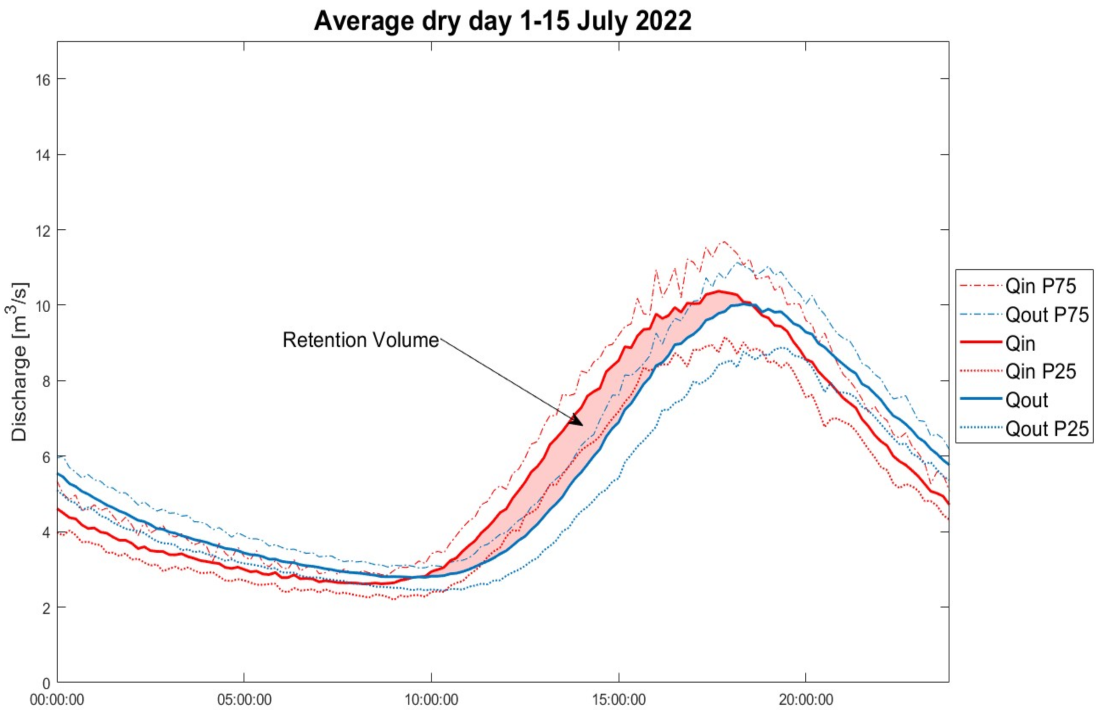

Figure A.5: Average dry day 1-15 July, 2022. Q_{IN} and Q_{OUT} hydrographs illustrating the average behavior of the Seracchi Lake inflows and outflows during a dry day occurred between 1-15 July 2022. The dashed lines represent the variability of the values from the mean, expressed in terms of the 75th percentile and 25th percentile.

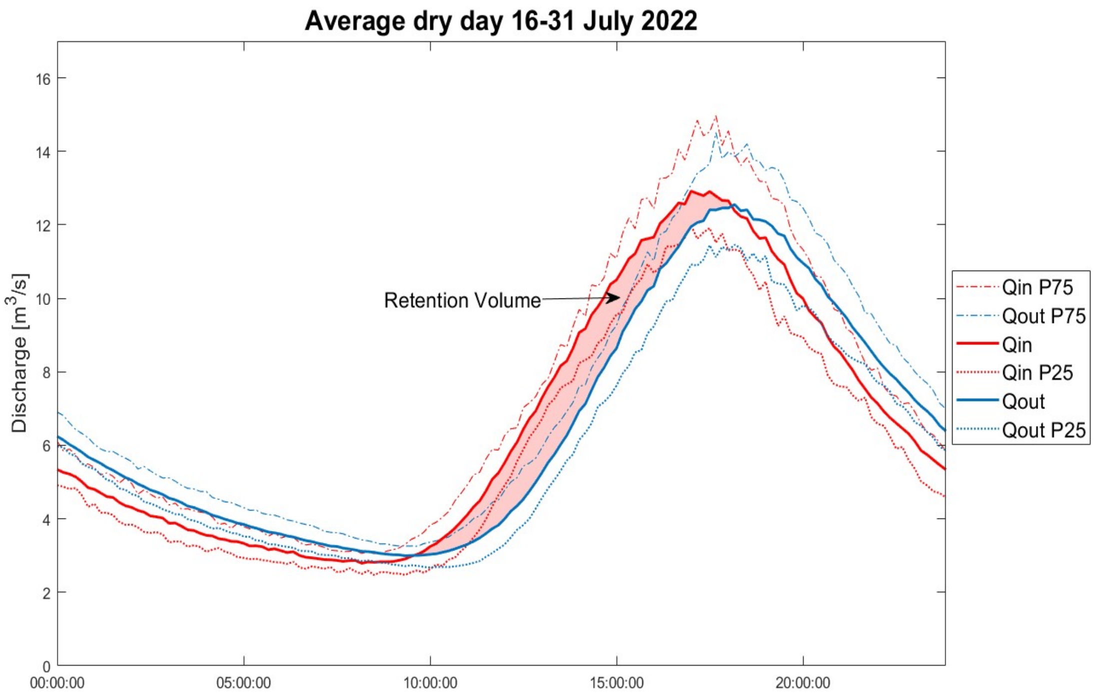

Figure A.6: Average dry day 16-31 July, 2022. Q_{IN} and Q_{OUT} hydrographs illustrating the average behavior of the Seracchi Lake inflows and outflows during a dry day occurred between 16-31 July 2022. The dashed lines represent the variability of the values from the mean, expressed in terms of the 75th percentile and 25th percentile.

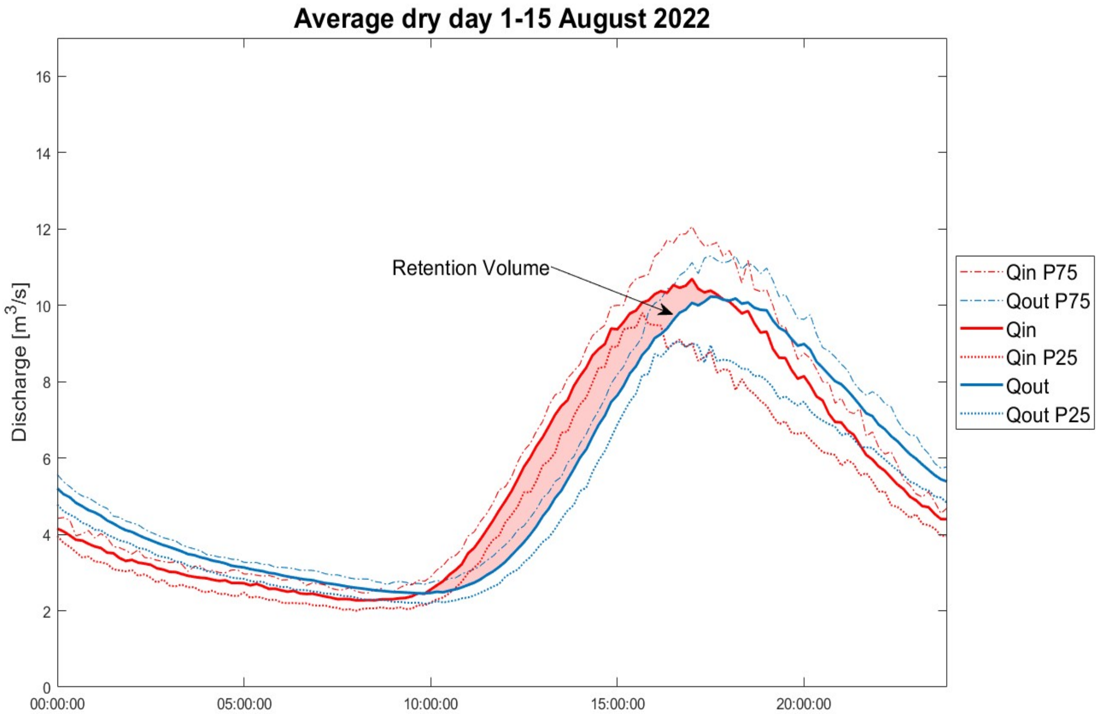

Figure A.7: Average dry day 1-15 August, 2022. Q_{IN} and Q_{OUT} hydrographs illustrating the average behavior of the Seracchi Lake inflows and outflows during a dry day occurred between 1-15 August 2022. The dashed lines represent the variability of the values from the mean, expressed in terms of the 75th percentile and 25th percentile.

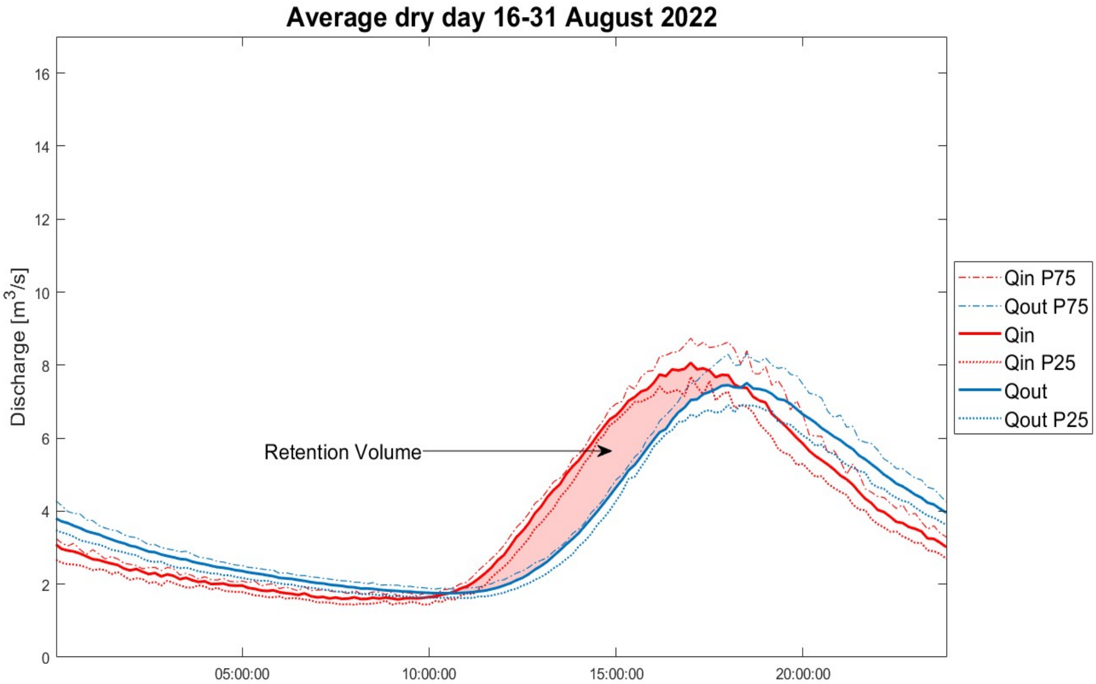

Figure A.8: Average dry day 16-31 August, 2022. Q_{IN} and Q_{OUT} hydrographs illustrating the average behavior of the Seracchi Lake inflows and outflows during a dry day occurred between 16-31 August 2022. The dashed lines represent the variability of the values from the mean, expressed in terms of the 75th percentile and 25th percentile.

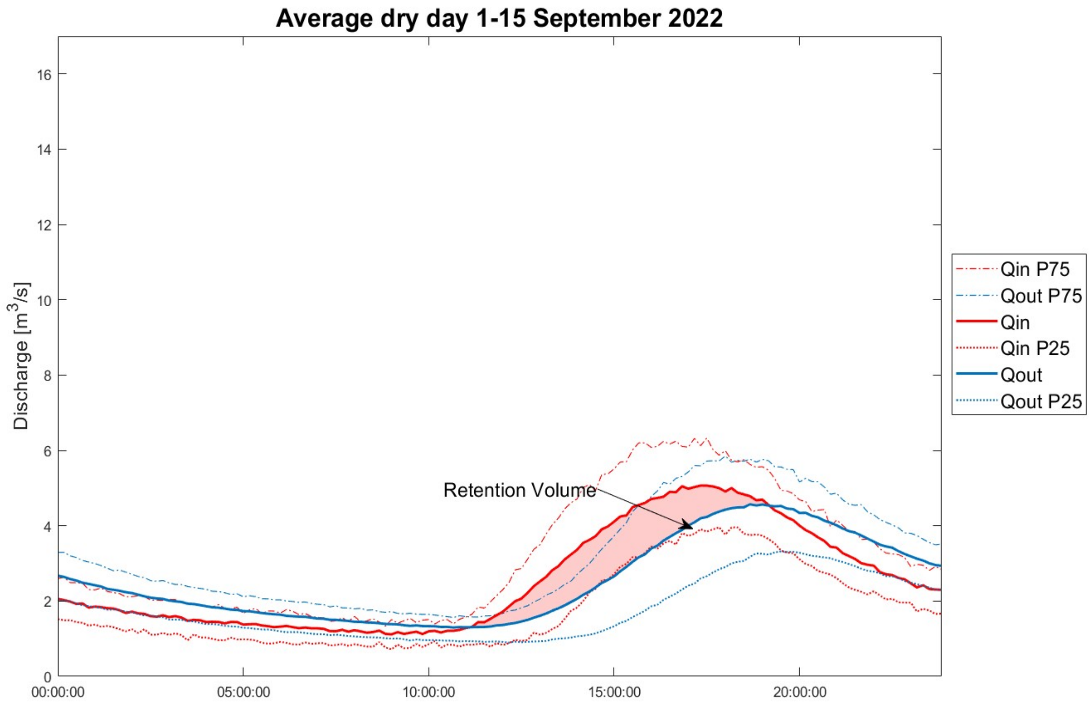

Figure A.9: Average dry day 1-15 September, 2022. Q_{IN} and Q_{OUT} hydrographs illustrating the average behavior of the Seracchi Lake inflows and outflows during a dry day occurred between 1-15 September 2022. The dashed lines represent the variability of the values from the mean, expressed in terms of the 75th percentile and 25th percentile.